Ca' Foscari
University
of Venice

Master's Degree programme

in Science and Technology of bio and Nanomaterials

Final Thesis

Synthesis and characterization of poly(DL-lactide-co-glycolide) nanoparticles with entrapped organic lanthanides and Yttrium complexes for imaging applications

Supervisor
Prof. Massimiliano Perduca

Assistant supervisor
Prof. Fabio Piccinelli

Graduand
Salvatore Calogero Gaglio
Matriculation Number 864200

Academic Year
2017 / 2018

Dedicated to my grandfathers

Acknowledgment

I sincerely thank the professors Massimilano Perduca and Fabio Piccinelli for their trust in me and my family for their supporting.

Abstract

Photoluminescence organic complexes of lanthanide ions show narrow band emission and high quantum yield, which make them interesting materials for fluorescence microscopy; moreover, their lifetime is milli second greater than conventional fluorophores (10^{-8}, 10^{-9} s) like fluorescein and rhodamine. Their potential application in biological system is limited by low solubility in water and toxicity of the metal. Water molecules are strong chelating agents of the lanthanide ions and cause decomplexation by hydrolysing the ligand with consequent loss of functionality: the mechanism of photoluminescence is based on the antenna effect. PLGA (poly[DL-lactide-co-glycolide]) nanoparticles holding complexes of lanthanide (Eu and Lu) ions have been synthetized to improve the solubility and produce a biocompatible material. PLGA is a co-polymer FDA approved and easily adsorbed by the cells. Also an isostructural organic complex of Yttrium has been encapsulated since this atom exhibits potential use in Positron Emission Tomography (PET), another imaging technique. The goal of the research was to produce PLGA nanoparticles with entrapped photoluminescence lanthanide complex and nanoparticles with Yttrium complex optimized for dimension, thermal stability and emission intensity (in the case of lanthanides), for possible in vitro and in vivo imaging.

INTRODUCTION **6**
PLGA NANOTECHNOLOGY 6
PHOTOLUMINESCENCE OF LANTHANIDES 9
IMAGING TECHNIQUES 12
EXPERIMENTAL SECTION **14**
MATERIAL 14
PREPARATION OF PLGA NANOPARTICLES (PLGA-NPS) 16
^{1}H-NMR SPECTROSCOPY 17
ELEMENTAL ANALYSIS 17
DYNAMIC LIGHT SCATTERING (DLS) AND ZETA POTENTIAL (ZP) 18
DIFFERENTIAL SCANNING CALORIMETRY (DSC) 18
ATOMIC FORCE MICROSCOPY (AFM) 18
LUMINESCENCE AND DECAY KINETICS 19
EMPTY PLGA NANOPARTICLES **20**
SIZE AND Z-POTENTIAL CHARACTERIZATION 20
TM EVALUATION 23
FLUORESCENCE ANALYSIS 24
DISCUSSION 25
LU(L1)$(NO_3)_3$ AND EU(L1)$(NO_3)_3$ EMBEDDED IN PLGA NPS **26**
SIZE AND Z-POTENTIAL CHARACTERIZATION 26
TM EVALUATION 28
FLUORESCENCE ANALYSIS 29
DISCUSSION 30
***RAC*-[EU(L1)(TTA)$_2$(H$_2$O)]$(NO_3)_3$ EMBEDDED IN PLGA NPS** **31**
SIZE AND Z-POTENTIAL CHARACTERIZATION 31
TM EVALUATION 34
FLUORESCENCE ANALYSIS 35
DISCUSSION 38
***RAC*-[EU(L2)(TTA)$_2$(H$_2$O)]CF$_3$SO$_3$ AND EUL3 EMBEDDED IN PLGA NPS** .. **39**
SIZE AND Z-POTENTIAL CHARACTERIZATION 39
TM EVALUATION 42
FLUORESCENCE ANALYSIS 43
DISCUSSION 48
***RAC*-[Y(L2)(TTA)$_2$(H$_2$O)]CF$_3$SO$_3$ EMBEDDED IN PLGA NPS** **49**
SIZE AND Z-POTENTIAL CHARACTERIZATION 49
TM EVALUATION 51
FLUORESCENCE ANALYSIS 52
DISCUSSION 53
CONCLUSION **54**
REFERENCES **55**
APPENDIX **59**

Introduction

PLGA Nanotechnology

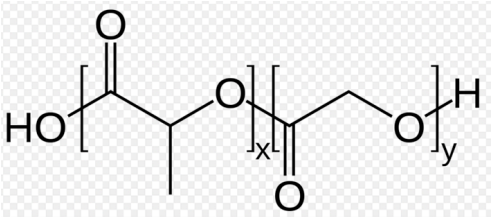

Figure. 1 Poly lactic-*co*-glycolic acid (PLGA): X = lactic moiety, Y = glycolic moiety

Poly lactic-*co*-glycolic acid (PLGA) is a copolymer of lactic acid and glycolic acid of remarkable interest for potential applications in biomedicine; indeed, for its biodegradability and biocompatibility, it is FDA and European Medicine Agency approved as drug delivery system for parenteral administration and also used in the biomedical industry as component of biodegradable sutures [1]. PLGA has been extensively studied as a carrier for the delivery of drugs, bioactive molecules, protein and other macromolecules such as DNA, RNA and peptides with potential application in tissue engineering, cardiovascular disease and cancer treatments, etc. [2,3] There are several variants of PLGA varying in molecular weight (10 kDa to 100k Da) and in the copolymer molar ratio (50:50, 75:25, 85:15 lactic/glycolic acid) with specific release profiles: increasing the amount of lactic acid, the crystallinity's degree increases with consequent high stability [4,5]. Therefore, molecular weight and copolymer molar ratio influence the degradation process and release profile of the drug entrapped: low molecular weight amorphous PLGA 50:50 shows faster release rate [6].

PLGA nanoparticles with definite physical-chemical properties can be synthetized changing the parameters (temperature, pH, concentration, etc.) of the method employed; there are several well-described methods of production adapted to various types of drugs, hydrophilic or hydrophobic small molecules or macromolecules. A commonly used method to prepare PLGA Nps is the single-emulsion method oil/water: the polymer is dissolved in an organic phase (e.g., dichloromethane, acetone, acetonitrile) and emulsified under stirring in an aqueous solution of a suitable surfactant (i.e.

polyvinyl alcohol, sodium dodecyl sulphate) [7]. Nanoparticles obtained are approximately of 200 nm; they should be able to avoid fast clearance by the reticuloendothelial system [8] and the rapid elimination through the kidneys. [9] This method allows to encapsulation of hydrophobic molecules simply dissolving them in the organic phase with the polymer, while in the case of hydrophilic molecules it is used the double-emulsion method oil/water/oil. [10] Thus, PLGA nanoparticles (NPs) not only protect the therapeutic agents with an increase of their stability, but also they can be used for controlled delivery of therapeutics improving pharmacokinetic and biodistribution profile, reducing the side effect [11]. In this context surface modification acquires an important rule. Generally, nanoparticles can passively reach the tumor exploiting the "Enhanced Permeability and Retention"(EPR) effect, a particular physiologic condition of the tumor vasculature [12]. Surface of PLGA Nps can be functionalized with ligands such as antibodies [13], aptamers, peptides, or small molecules, that for example can recognize tumor-specific antigens, to provide an active targeting towards specific organs or cells [14, 15]. Thus, nanoparticles are targeted to the extracellular portion of the transmembrane antigens and then taken up by the cells through receptor-mediated endocytosis [16]: the absorption is enhanced with a consequent increase in the concentration *in situ* of the drug encapsulated, allowing to reduce the initial administration and avoiding to promote side effects. Moreover, the nanoparticle surface is usually stabilized by conjugation of polyethyleneglycol (PEG), to extent systemic circulating half-life: indeed, PEG prevents the process of opsonisation extending systemic circulating half-life [17, 18]. For example, in Sun Hwa Kim *et al.* PLGA nanoparticles were surface coated with cationic di-block copolymer, poly(L-lysine)-poly(ethylene glycol)-folate (PLL-PEG-FOL) conjugate, to promote specific site targeting by exploiting overexpressed tumor cell receptors and to produce a *stealth* drug-delivery system [19]; the surface was functionalized through an ionic bond between the positive charge of the poly(L-lysine) and the negative one of the nanoparticle surface. The release of the drug can be triggered by internal or external stimuli [20] such as changes in pH, temperatures [21], or the presence of an analyte such as glucose [22]: Naik et al. were able, through a local heating by microwave irradiation of a magnetic iron core contained in PLGA nanoparticles, to increase the rate of release [23]. Therefore, through the functionalization allows designing a PLGA

nanocarrier with controlled release, active targeting and long permanence in the blood system, which are able to improve the pharmacokinetics and the therapeutic efficacy reducing the adverse effects.

PLGA nanoparticles could also be used as a diagnostic tools by encapsulating dyes or contrast agents useful for imaging application: indeed, several visible [24, 25, 26] and NIR-emitting [27, 28] organic dyes have been successfully encapsulated and employed in in-vivo experiments. Furthermore, multifunctional PLGA nanoparticles able to carry both drugs and dyes (or contrast agent) have been designed for theranostic purpose [29, 30]: thus, it is possible following the biodistrubution and accumulation of the drug encapsulated *in-vivo* studies. A. Topete *et al.,* report a PLGA device able to detect traumatic brain injures using fluorescence imaging and ^{19}F magnetic resonance imaging: NIR-emitting dyed (IRDye 800CW) and Perfluorocarbon (PFC, ^{19}F) were encapsulated together in PLGA NPs. Encapsulating in these nanoparticles, for example, a regenerative drug, it could be possible to develop a nanocarrier able to carry out diagnosis and therapy at the same time (theranostic) [31]. In conclusion, Poly lactic-*co*-glycolic acid is an interesting biomaterial for potential application in the field of medicine. Lastly, the ability to protect drugs (or imaging agents) and to modulate the physicochemical proprieties with the synthesis and functionalization, make PLGA a versatile material for multiple applications in medicine.

Photoluminescence of lanthanides

Luminescence includes a series of phenomena in which, following an excitation, a substance decays in its fundamental state emitting an electromagnetic wave: specifically, it is called photoluminescence when the excitation involves the absorption of a radiation. The emitted radiation has normally a lower energy than the excitation one due to non-radiative decays (Stokes' shift).

The lanthanides are elements where the 4*f* (and 5*f*) orbitals are gradually filled. At the fundamental state all these elements are presented as strongly electropositive metals and classified as hard acids according to *Hard and Soft Acid and Bases* Pearson's theory; indeed, Lanthanides form stable complexes primarily with anionic hard species (mono or polydentate ligands), particularly oxygen- and nitrogen-donors. Moreover their most stable oxidation state is 3+, although 2+ or 4+ are possible for some Lanthanides in specific conditions. The electric and magnetic properties of the lanthanides are determined by the *f* orbitals: they are not involved in the bonding formation with ligands and thus the electric and magnetic properties are substantially unperturbed by the surrounding environment. Due to the inefficient shielding of the nucleus by the 4f orbitals, there is a gradual decrease of the radii of the trivalent ions Ln^{3+} with the increase of the atomic number Z, a trend known as "lanthanide contraction": thus neighbouring lanthanides have similar, but not identical, properties. Furthermore this contraction makes the radius of Y^{3+} similar to the radii of some lanthanides; as a consequence, the coordination chemistry of Yttrium is usually compared to that of rare earths, despite the different electronic properties due to different atomic numbers [32].

Due to the relative independence of the *f* orbitals from the surrounding environment the photoluminescence of the *f-f* transitions shows narrow emission bands. However, these transitions are forbidden by Laporte's rule of parity and the absorptions are characterized by low values of molar extinction coefficients (around 10 M^{-1} cm^{-1}): this is the reason why lanthanides salts have low emission spectra. To improve photoluminescence process lanthanides organic complexes are synthetized, in which ligands, acting as a sensitizer (or antenna), absorbs a suitable wavelength of radiation and then transfer the excitation to the lanthanide ion (figure 2). Generally these ligands

are N-donor or O-donor species with π-π aromatic rings. Therefore the donor (organic chromophore) absorbs a photon passing to the excited state of singlet after, through the intersystem crossing conversion the state of triplet is populated from which usually the energy is transferred to the acceptor (lanthanide). Energy transfer can occur through two main mechanisms:

- Dexter energy transfer [33] consisting of a double electronic exchange between donor and acceptor;
- Forster energy transfer (FRET) [34] involving a dipole-dipole interaction between donor and acceptor.

Both these mechanisms are negatively influenced by increasing donor-acceptor distance, an example, in FRET mechanism the effectiveness of transfer is proportional to R^{-6}, where R is the distance between donor and acceptor. Due to overlapping orbitals condition for DEXTER process, FRET is considered the most probable mechanism to energy transfer [35] for lanthanide ions.

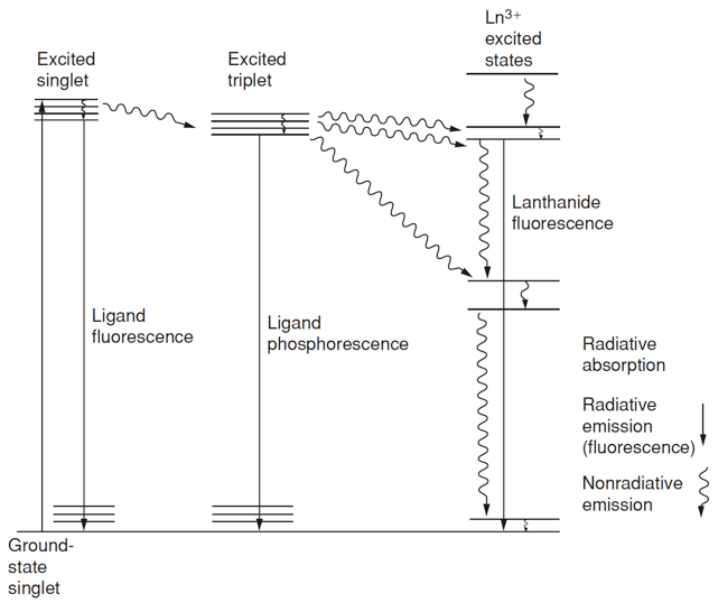

Figure 2. Jablonski diagram illustrating the antenna effect

Fluorescence intensity depends not only on the efficacy of energy transfer but also on the presence of non-radiative quenching phenomena, indeed, for example in aqueous

solution another path for terminating the excited state of lanthanide is available, in the form of vibrational energy transfer to water molecules, that phenomenon is called multi phonon relaxation [36, 37] (figure 3 shows this process in Eu(III)). This turning off of Fluorescence can be reduced working in solid state or in non-aqueous solvents or using multidentate ligands that exclude waters from the sphere of coordination of the metal.

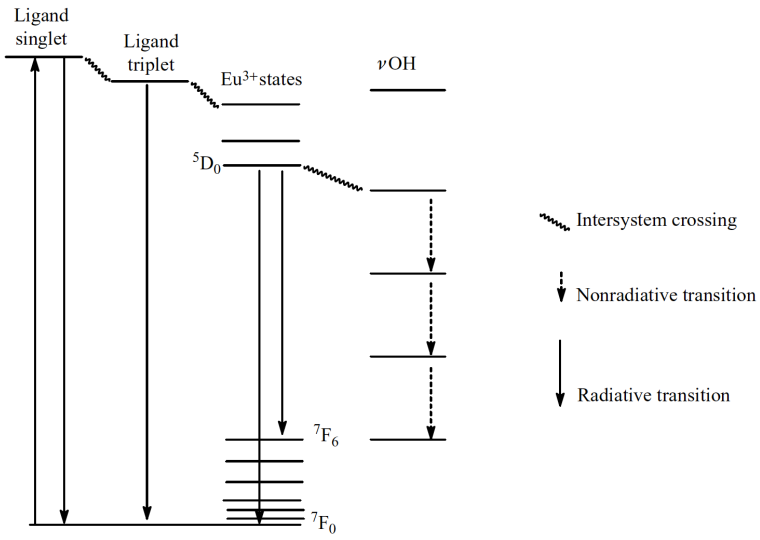

Figure 3. Quenching of Eu(III) luminescence through multiphonon relaxation of OH groups

In addition the lanthanide complexes are also affected by the concentration quenching in which, exceeding certain concentration values, the fluorescence intensity decrease [32].

For the narrow-size luminescence that the complexes with rare earth antenna binders show and thanks to the long life time of the luminescence itself, these species are employed such as: diagnostic tool, sensors and luminescent probes for various biomolecules, base for making OLEDs and so on [38].

Imaging techniques

The term imaging refers to the set of medical diagnostic procedures (eg radiography, ultrasound, magnetic resonance imaging, optical imaging) with the aim of producing images that visualize anatomical structures or physiological processes, to identify malformations or diseases.

Among these the Positron Emission Tomography (PET) is a diagnostic tool of nuclear medicine used often for the detection of tumors such as liver cancer. It is based on the emission of positrons that annihilate with the electrons of the body producing a small amount of energy in the form of two photons that are emitted in opposite directions. The PET detection system measures these photons and uses this data to make images of the internal organs. An example is found in Attarwala *et al*. where the low decay positron emission of ^{90}Y was used to detect liver tumor via PET imaging [39].

In the field of the optical imaging, nano-sized agents have been very successful as they are more stable and brighter than the usual organic chromophores. In this context an interesting role is given to nanoparticles not only for their carrier and protection function of the dye but also because through surface modification they are able to label specific cells or tissues. Nano-sized imaging agents can be classified into two categories based on their chemical nature and synthesis method: hard nanomaterials (e.g. quantum dots dye-doped silica NPs, carbon NPs), and soft nanomaterials (e.g. polymeric NPs as PLGA, micelles). Another interesting difference is that almost all hard nanomaterials are bio-incompatible due to their inorganic nature while soft optical nano-sized imaging agents are fabricated from less toxic organic molecules and more of them are FDA approved. So in vivo studies soft nano-sized imaging agents take a central role [40]. In the design of an nano-sized imaging agent, the dimensions are important: indeed, it has been shown that nanoparticles with dimensions smaller than 200 nm are easily internalized by the cells and they can accumulate inside the cancer cells by enhanced permeation and retention effect (EPR). Moreover, to obtain superior brightness a strong dye loading without aggregation-caused quenching (ACQ) is required. ACQ is a very real problem and it is responsible for wrong interpretations of data in the quantitative

analysis of whole-body optical imaging [41]. To avoid misleading observations in whole-body fluorescence imaging of NP distribution, it is important to verify that fluorescence dyes do not quench in NPs and the fluorescence intensity increases linearly with the NP concentration. Only recently several strategies of dye design were proposed to overcome ACQ in polymer NPs. In particular, aggregation induced emission (AIE) and dye modification with bulky side groups and use of bulky hydrophobic counterions [42]. Finally, due to the possibility of obtaining nanoparticles with dimensions below 200 nm able of active targeting with a moldable pharmacokinetic, PLGA is an excellent basis for the construction of nano-sized agents for imaging purpose.

Experimental Section

Material

PLGA (poly[DL-lactide-co-glycolide],50:50/75:25 lactide-glycolide ratio, CAS 26780-50-7), ethanol (≥99% purity, CAS 64-17-5), PVA (poly[vinyl alcohol], CAS 9002-89-5), SDS (sodium dodecyl sulfate)(CAS 151-21-3), Sodium cholate (CAS 206986-87-0), Glycine (CAS 56-40-6) Citric acid (CAS 5949-29-1), Sodium acetate (CAS 127-09-3) Dichloromethane (CAS 75-09-2) were purchased from Sigma Aldrich. Acetone (≥99% purity, 1.00013.) was purchased from Merck.

The complexes (Aldrich, 98%) were stored under vacuum for several days at 80°C and then transferred in a glove box.

N, N'-bis(2-quinolylmethylidene)- 1,2-(R,R+S,S)-cyclohexanediamine (**L1**) *N, N'-bis(2-pyridylmethylidene)- 1,2-(R,R+S,S)-cyclohexanediamine* (**L2**), and *N-quinolyl-N,N',N'-trans-l,2-cyclohexylenediaminetriacetic acid* (**L3**) were synthetized by following the procedures reported in literature [43,44], as well as the complexes Eu or Lu(**L1**)$(NO_3)_3$, Eu(**L3**) [46] and *rac*-[Eu(**L2**)$(tta)_2(H_2O)$] CF_3SO_3 [45] (Figure 4). Finally *rac*-[Eu(**L1**)$(tta)_2(H_2O)$] $(NO_3)_3$] was synthetized flowing the same protocol of *rac*-[Eu(**L2**)$(tta)_2(H_2O)$], changing the ligand.

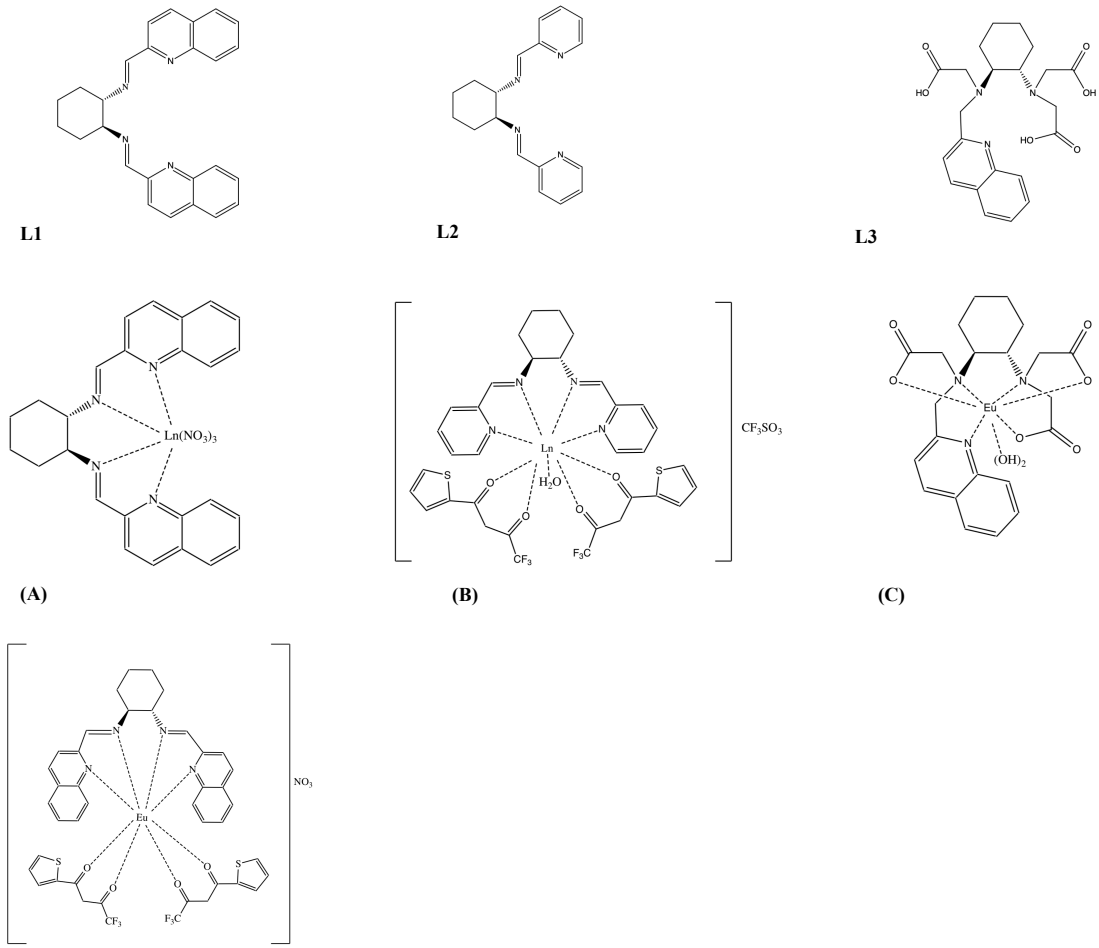

Figure 4. Molecular structure of the ligands and complexes under investigation: **(A)** (Eu or Lu)(**L1**)$(NO_3)_3$; **(B)** *rac*-[(Eu or Y)(**L2**)$(tta)_2(H_2O)$] CF_3SO_3; **(C)** Eu(**L3**) ; **(D)** *rac*-[Eu(**L1**)$(tta)_2(H_2O)$] $(NO_3)_3$];

rac-[Y(**L2**)$(tta)_2(H_2O)$] CF_3SO_3 was synthesized as follows: at room temperature, 78 mg (0,342 mmol) of Htta have been dissolved in a methanol (2mL) solution containing 19 mg (0.342 mmol) of KOH. The clear solution was slowly added to a methanol solution (2ml) of the ligand **L2** [50 mg (0,171 mmol)] and $Y(CF_3SO_3)_3{\cdot}6H_2O$ [101 mg (0,171 mmol)]. The final mixture was stirred for 1 hour at room temperature and then the solvent was removed under reduced pressure. The desired product has been obtained in a good yield as white powder upon extraction in dichloromethane (6 mL) followed by the removal of the solvent under reduced pressure.

Rac-[Y(**L2**)(tta)$_2$(H$_2$O)]·CF$_3$SO$_3$: Yield 65%. ^{1}H-NMR (CDCl$_3$) δ (ppm): 8.74 (s, 2H HC=N), 8.69 (d, J=4.70 Hz, 2H Py), 8.07 (m, 4H, Py), 7.69 (d, J=4.92 Hz, 2H, Py), 7.64 (d, J=3.13 Hz, 2H, thiophene), 7.56 (d, J=4.25 Hz, 2H, thiophene), 7.13 (t, J=4.25 Hz, 2H, thiophene), 4.27 (m, 2H, "CH" cyclohexane), 3.51 (m, 1H, cyclohexane), 2.75 (m, 2H, cyclohexane), 2.21 (m, 2H, cyclohexane), 1.89-1.50 (m, 3H; cyclohexane).
Elemental Anal. Calc. for $C_{35}H_{32}EuF_9N_4O_8S_3$ (MW 992.7): C, 42.01.82; H, 3.05; N, 5.58; O, 12.77; S 9.59. Found: C, 42.34 ; H, 3.25; N, 5.64; O, 12.89; S 9.69. UV-Vis absorption spectroscopy (acetonitrile): ε(280 nm): 64600 $M^{-1}cm^{-1}$; ε(350 nm): 65600 $M^{-1}cm^{-1}$.

Preparation of PLGA nanoparticles (PLGA-Nps)

PLGA-Nps were prepared by classic single emulsion method (o/w) and modified single emulsion method using sonication (MICROSON^{TM} Ultrasonic Cell Disruptor) at 20°C [10] 10 mg of PLGA were dissolved in 1 mL of organic solution (85% acetone and 15% ethanol), then the obtained solution was added dropwise to 10 mL of aqueous solution (surfactant, buffer, table 1) and emulsified through stirring (classic method) or through 3 cycles of sonication (power 8 RMS for 10s with rest 5s/cycle). In each case, the emulsion was stirred (2000 RPM) *overnight* at 20°C to evaporate the organic phase.
Afterwards, samples were centrifuged at 4°C 11000 rpm for 15 minutes (Eppendorf Centrifuge 5804 R): the pellet was suspended in 5mL of Milli-Q water and centrifuged again. Finally, the purified nanoparticles were suspended in 1 mL of PBS solution pH 7,4 (or Milli-Q water) for the subsequent analysis and the storage at 4°C, otherwise suspended in 1 mL of PBS added with mannitol 4% as a cryoprotectant for lyophilisation. Nanoparticles with both polymeric combinations Poly(lactic(50%)-co-glycolic acid(50%), briefly PLGA 50:50 and Poly(lactic(75%)-co-glycolic acid(25%), briefly PLGA 75:25, were prepared using the same method.
In the case of PLGA nanoparticles with entrapped complexes, these were dissolved together with PLGA in the organic solution (85% acetone and 15% ethanol). The following steps were the same of the method above.

Surfactant
Sodium dodecyl sulphate (SDS)
Poly(vinyl alcohol) (PVA)
Sodium cholate

Buffer (100 mM)
Glycine-NaOH pH 9
Citric acid-NaOH pH 3
Sodium acetate-HCl pH 5

Table 1. Surfactants and buffer solutions used in the different synthesis protocols

^{1}H-NMR spectroscopy

Nuclear magnetic resonance (NMR) experiments were performed at 298.15 K using a 600 MHz Bruker Avance III spectrometer equipped with a triple resonance TCI cryogenic probe. Spectra were usually recorded in $CDCl_3$ and, unless otherwise noted, chemical shifts are expressed as ppm and referenced to the internal standard tetramethylsilane (TMS). One dimensional NMR spectra were recorded with 8 or 16 scans and a spectral width of 12019 Hz. All spectra were manually phased and baseline corrected using TOPSPIN 3.2 (Bruker, Karlsruhe, Germany). Chemical shift, multiplicity (s, singlet; d, doublet; t, triplet; m, multiplet; b, broad), coupling constants and integration area are reported.

Elemental analysis

Elemental analysis were carried out by using a EACE 1110 CHNOS analyzer.

Dynamic Light Scattering (DLS) and Zeta Potential (ZP)

A first analysis was performed at room temperature with a Zeta NanoSizer in PBS buffer to measure the size and Z-potential. The samples were diluted 10 times from the stock solutions to perform each analysis.

Differential Scanning Calorimetry (DSC)

These analyses were performed in Milli-Q water to evaluate the melting temperature (Tm) of the polymeric matrix containing the complexes. In particular, 700 μL of each sample were loaded in the sample cell, while the same volume of Milli-Q was loaded in the reference one. A scanning was performed from 10°C to 90°C (2°C/min): finally, Tm was calculated using the program Lauch NanoAnalyze. Data were fitted with Gaussian function to calculate the relative melting point with 99% of confidence.

Atomic Force Microscopy (AFM)

20μL of each sample (described in the above section) was loaded on a bracket covered by inert mica surface. After 15 minutes for solvent evaporation, the analysis was performed using semi contact mode with different scanning frequencies (3 to 1 Hz) to obtain the greatest AFM image; finally, the images were elaborated with the program Gwyddion and GUI program [47] and statistical study was performed to compare results to DLS data. However the statistics of the second program provides the nanoparticle areas as output, hence the diameter has been calculated by applying $d=2\cdot\sqrt{(A/\pi)}$ equation (approximation of the equatorial area): where d is the diameter and A is the equatorial surface of the nanoparticle.

Luminescence and decay kinetics

The emission intensity was recorded in PBS, with medium sensitivity, using a Jasco Spectrofluorometer FP-8200 and exciting the samples at 360 nm for [Eu or Lu(**L1**)$(NO_3)_3$] and *rac*-[Eu(**L1**)(tta)2(H2O)]$(NO_3)_3$, at 350 nm *rac*-[Eu or Y(**L2**)$(tta)_2(H_2O)]\cdot CF_3SO_3$ and at 320 nm for [Eu(**L3**)]. These are the greatest excitation wavelengths to achieve an efficient antenna-effect with high consequent emission [43,45,46]. Moreover, for both variants of PLGA nanoparticles with entrapped *rac*-[Eu(**L1**)(tta)2(H2O)]$(NO_3)_3$ and *rac*-[Eu(**L2**)$(tta)_2(H_2O)]\cdot CF_3SO_3$, the emission intensity over time were studied at 20°C and 37°C: in each case, samples were diluted from the stock solution to have the signal stay in to the machine sensitivity range. Only for *rac*-[Eu(**L2**)$(tta)_2(H_2O)]\cdot CF_3SO_3$ were investigated the lifetimes: therefore, in decay kinetics measurements, a Xenon microsecond flashlamp (Fluorolog 3 (Horiba-Jobin Yvon) spectrofluorometer) was used and the signal was recorded by means of multichannel scaling method. True decay times were obtained using the convolution of the instrumental response function with an exponential function and the least-square-sum-based fitting program (SpectraSolve software package). The total quantum yields (ϕ_{Tot}) have been obtained by secondary methods described in literature [48] by measuring the visible emission spectrum of quinine bisulfate in 1N H_2SO_4 solution, a fluorescence quantum yield reference sample (ϕ = 54.6%). ϕ_{Tot} for the complexes has been calculated by $[(A_s\cdot F_u\cdot n^2)/(A_u\cdot F_s\cdot n_o^2)]\cdot \phi_s$ equation; where: u subscript refers to unknown and s to the standard and other symbols have the following meanings: ϕ is quantum yield, A is absorbance at the excitation wavelength, F the integrated emission area across the band and n's are respectively the refraction index of the solvent containing the unknown (n) and the standard (n_0) at the sodium D line and the temperature of the emission measurement.

Empty PLGA nanoparticles

Size and Z-potential characterization

Different formulations have been adopted by changing not only the synthesis parameters (Surfactant, Temperature of synthesis, pH, concentration) but also the emulsification system, to evaluate their effect on particle size. Table 2 shows the DLS results (Z-average, PDI, St-deviation) for the empty synthesized PLGA nanoparticles with simple-emulsion method under stirring; while table 3 shows the DLS results for the same nanoparticles prepared using sonication as emulsification system. F2 (PLGA [50:50] nanoparticles) and F4 (PLGA [75:25] nanoparticles) were the best formulation in terms of size (179,6 nm and 182,4 nm), PDI and stability with a Z-potential of -10,14 mV and -4,47 mV respectively. These preparations were further characterized with AFM, DSC and fluorescence spectroscopy. No DLS signals were detected increasing the concentration of PVA to 2% either decreasing the concentration of PLGA to 5 mg/ml, moreover the same result was seen for the preparation under sonication (S1 and S2). Using SDS as surfactant the size has been reduced to 145,5 nm but this nanoparticles were affected by aggregation due to the high value of Z-potential (-35 mV) while, with the sodium cholate, synthesized nanoparticles were not mono-dispersed despite an optimum potential of -6.73 mV; on the other hand, the synthesis conducted under sonication did not bring any result. An example of DLS diagram is reported in figure 5: as can be seen, the nanoparticles are distributed around 140 nm with a standard deviation of 48,19 nm.

Formulation	Surfactant (%)	PLGA (Mg/ml)	T (°C)	pH	Solvent (%)	Z-a (nm)	PDI	St-dev (nm)
F1.	PVA 0,5	[50:50] 10	20	7,5	Acetone/ethanol 85/15	178	0,038	48,19
F2.	PVA 1	[50:50] 10	37	9	Acetone/ethanol 85/15	179,6	0,123	48,19
F3.	PVA 1	[50:50] 5	37	9	Acetone/ethanol 85/15	-	-	-
F4.	PVA 1	[75:25] 10	37	9	Acetone/ethanol 85/15	182,4	0,082	47,57
F5.	PVA 2	[50:50] 10	37	9	Acetone/ethanol 85/15	-	-	-
F6.	SDS 2	[50:50] 10	37	9	Acetone/ethanol 85/15	145,5	0,147	52,3
F6	Sodium Cholate 2	[50:50] 10	37	9	Acetone/ethanol 85/15	129,7	0,343	50,07

Table 2. Formulations and DLS results (Z-average, PDI, st-deviation) of empty PLGA nanoparticles synthetized by stirring

Formulation	Surfactant (%)	PLGA (Mg/ml)	T (°C)	pH	Solvent (%)	Z-a (nm)	PDI	St-dev (nm)
S 1.	PVA 1	[50:50] 10	37	9	Acetone/ethanol 85/15	-	-	-
S 2.	PVA 1	[75:25] 10	37	9	Acetone/ethanol 85/15	-	-	-

Table 3. Formulations and DLS results (Z-average, PDI, st-deviation) of synthetized empty PLGA nanoparticles by sonication

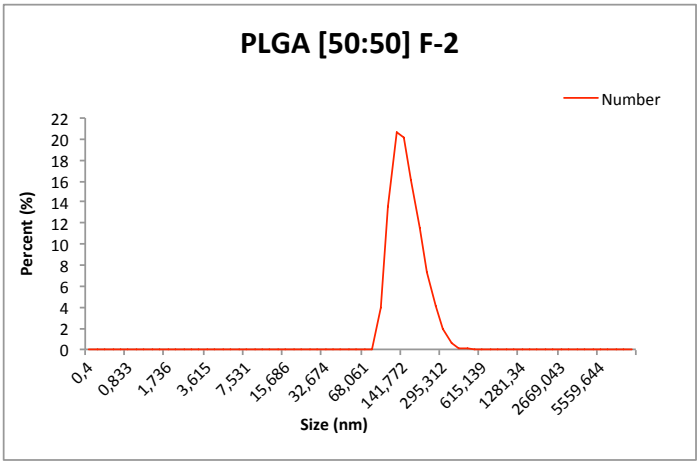

Figure 5. DLS diagram of empty PLGA 50:50 (sample F2) dispersed in PBS. The size reported in table 2 is the average value calculated on three different samples.

To confirm the size results of F2 and F4, the nanoparticles have been analysed by AFM and the images were processed with the GUI program on Mathlab platform. An example of that is shown in figure 6, where a clear aggregation of nanoparticles with spherical shape is visible due most probably to sample preparation. Furthermore, to run an accurate statistical analysis it was necessary concentrate the sample to obtain as wide population as possible.

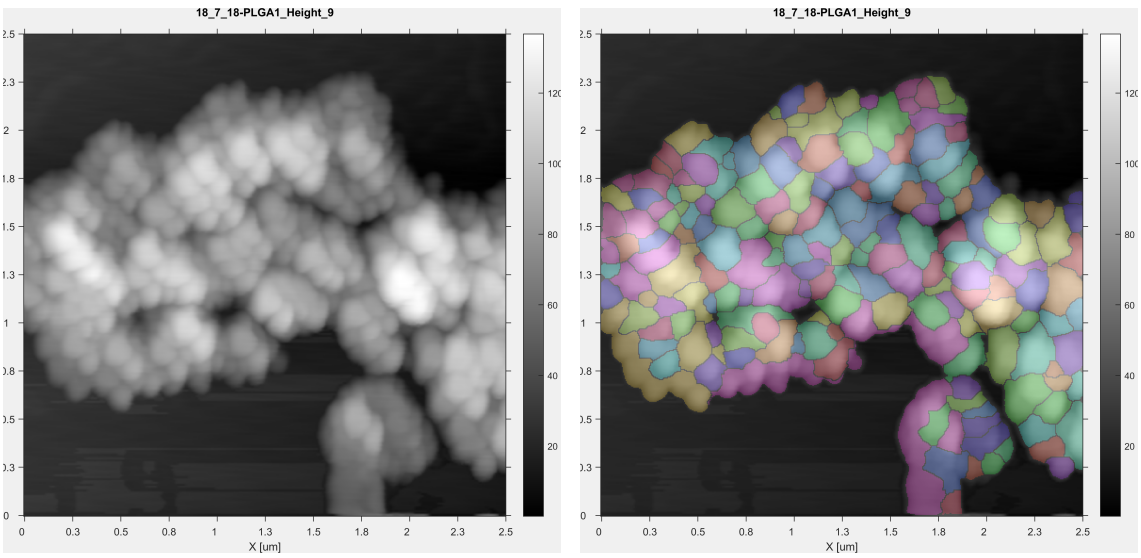

(**A**) (B)

Figure 6. (A) AFM image of PLGA [50:50] (F2) processed by GUI program; **(B)** application of Watershed algorithm

Simple	Population	GUI statistics (nm)	DLS size (nm)
F2	125	152,76 ± (36,44)	179,6 ± (48,19)
F4	122	182,9 ± (46,77)	182,4 ± (47,57)

Table 4. Comparison between DLS data and AFM statistic

Tm evaluation

To evaluate the thermal stability, samples (F2 and F4) were suspended in Milli-Q water and the melting temperature (Tm) was calculated using a Gaussian approximation with 99% of Confidence Level (29,14 ± 0,101 °C for [50:50] and 33,99 ± 0,046 °C for [75:25]); in figure 7 is reported an example of the DSC data with the calculation of Tm for the F1.

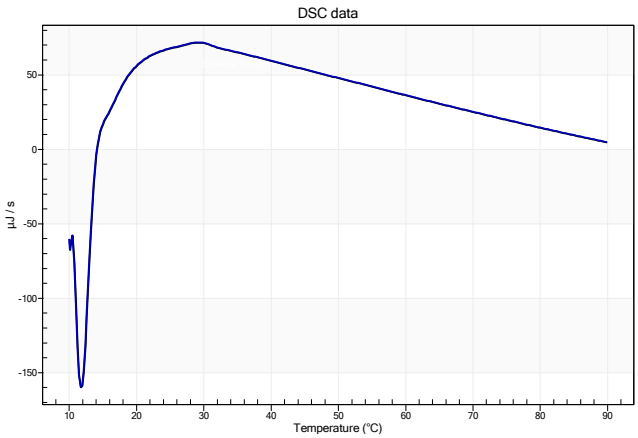

(A)

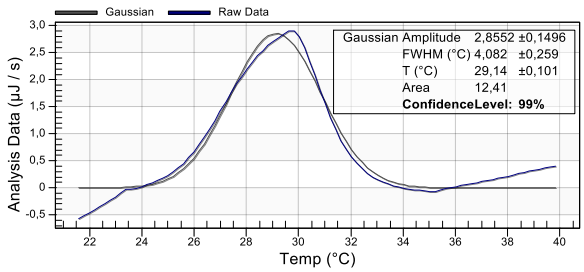

(B)

Figure 7. (A) DSC data of F1 in which is visible a weak peak around the Tm point. **(B)** Calculation of Tm using Gaussian approximation with 99% of Confidence Level.

Fluorescence analysis

PLGA nanoparticles were investigated in emission spectroscopy using three different excitation wavelengths (320, 350 and 360 nm) without getting any result (data not show)

Discussion

Nanoparticles of empty PLGA, F2 and F4, show the best results for size (179,6 nm and 182,4 nm), Z-potential and poly dispersion index: instead, the use of sonication do not allow the formation of nanoparticles (absence of DLS signal). For F4 the DLS data is confirmed by AFM statistic, while for F2 the little difference is probably due to the amorphous characteristic of PLGA [50:50]. Indeed, as a soft material, these nanoparticles could undergo a process of dehydration, more stressed in [50:50] than [75:25] probably for different crystalline degree, caused by the method of preparation for the analysis. In addition, the watershed algorithm fails to effectively highlight the individual nanoparticles due to the aggregation. The melting temperature (Tm) is related to the breaking of weak interactions such as dipole-dipole, Van Der Walls and hydrogen bond interactions responsible of the assembly of the nanoparticles: the [75:25] system, containing a higher quantity of the poly-lactic component, is more thermally resistant than the 50:50 ones. For this reason, F4 and F2 show different melting temperatures, around 34°C and 29°C, respectively.

Lu(L1)$(NO_3)_3$ and Eu(L1)$(NO_3)_3$ embedded in PLGA NPs

Size and Z-potential characterization

In PLGA nanotechnology it is very common that, trying to encapsulate something, the system's response to the synthesis parameters changes: therefore, different formulations have been tried changing the Temperature, pH, the concentration of PLGA, of the complex and of the PVA. In this case the criterion selection was to obtain as small nanoparticles as possible with high emission intensity. Lu(**L1**)$(NO_3)_3$ and Eu(**L1**)$(NO_3)_3$ show an intense emission around 440 nm and 616 nm respectively, upon excitation at 360 nm [43]. Despite the several formulations employed, it was only possible to reduce the size without recording any emission for both complexes: for simplicity it is reported only the formulations employed to encapsulate Lu(**L1**)$(NO_3)_3$, the same for both complexes (table 5). Almost all preparations were affected by aggregation; only F[LuL1]-14 and F[LuL1]-15 allowed to obtain stable nanoparticles in solution, PBS or Milli-Q water with -2,3mV and -4,3 mV as a Z-potential. Since these complexes are iso-structural, the same results have been verified for Eu(**L1**)$(NO_3)_3$. AFM analysis was not performed.

Form.	PVA (%)	PLGA (Mg/ml)	Complex	T (°C)	pH	Solvent (%)	Z-a (nm)	PDI	St-dev (nm)
F[Lu**L1**]-1	0,5	[50:50] 10	2	20	7,5	Acetone/ethanol 85/15	344,1	0,12	132,2
F[Lu**L1**]-2	1	[50:50] 10	2	20	7,5	Acetone/ethanol 85/15	304,1	0,12	111
F[Lu**L1**]-3	1	[50:50] 10	1	20	7,5	Acetone/ethanol 85/15	277,8	0,08	80,2
F[Lu**L1**]-4	1	[50:50] 10	1	20	7,5	Acetone/ethanol 85/15	276,3	0,10	86,62
F[Lu**L1**]-5	1	[50:50] 10	1	20	7,5	Acetone 100	294,2	0,09	77,91
F[Lu**L1**]-6	1	[50:50] 10	1	20	7,5	Acetone 100	304,7	0,11	109,3
F[Lu**L1**]-7	1	[50:50] 10	1	37	7,5	Acetone/ethanol 85/15	259,4	0,1	85,97

F[Lu**L1**]-8	1	[50:50] 10	1	4	7,5	Acetone/ethanol 85/15	297,9	0,15	95,29
F[Lu**L1**]-9	1	[50:50] 10	1	20	3	Acetone/ethanol 85/15	248	0,12	85,12
F[Lu**L1**]-10	1	[50:50] 10	1	20	5	Acetone/ethanol 85/15	254,7	0,15	94,47
F[Lu**L1**]-11	1	[50:50] 10	1	37	3	Acetone/ethanol 85/15	236	0,08	69,62
F[Lu**L1**]-12	1	[50:50] 10	0,5	37	3	Acetone/ethanol 85/15	225,3	0,01	52,48
F[Lu**L1**]-13	1	[50:50] 10	1	37	9	Acetone/ethanol 85/15	215,4	0,06	57,57
F[Lu**L1**]-14	1	[50:50] 10	0,25	37	9	Acetone/ethanol 85/15	203,6	0,11	60,5
F[Lu**L1**]-15	1	[75:25] 10	0,25	37	9	Acetone/ethanol 85/15	199	0,06	51,8

Table 5. Formulations and DLS results (Z-average, PDI, st-deviation) of PLGA[Lu(**L1**)$(NO_3)_3$] nanoparticles synthesized by stirring.

Tm evaluation

Despite the absence of emission, the melting temperature was anyway calculated for F[Lu**L1**]-14 and F[Lu**L1**]-15 NPs. Interestingly, for both protocols the nanoparticles show an increased thermal stability, more o less 4 °C than the empty ones (38,6 ± 0,029 °C for [75:25] and 34,21 ± 0,053°C for [50:50]) (figure 8).

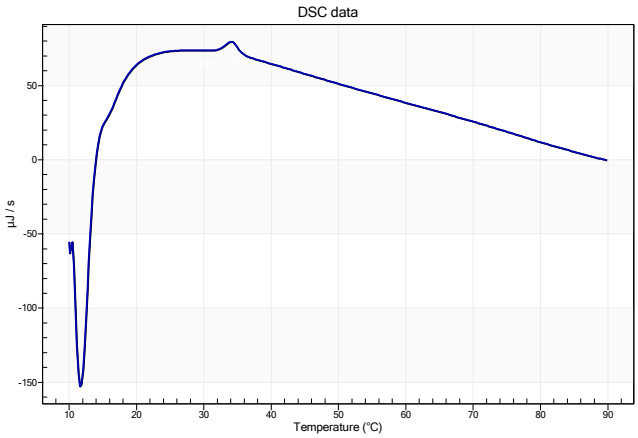

(A)

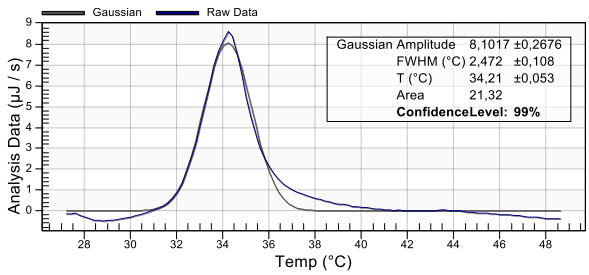

(B)

Figure 8. (A) DSC data of F[Lu**L1**]-14 nanoparticles in which is visible a peak around the Tm point. **(B)** Calculation of Tm using Gaussian approximation with 99% of Confidence Level.

Fluorescence analysis

As described above the complexes have been encapsulated in PLGA NPs losing their emission ability, an evidence for this phenomenon is explained in figure 9: Eu(**L1**)$(NO_3)_3$ dissolved in the reaction solvent (acetone 85% ethanol 15%) shows the relative fluorescence at 616 nm (red line) upon excitation at 360 nm while the complex embedded in PLGA NPs in PBS (blue line) did not show the expected peak. Only the ligand emission is detected around 410 nm [43].

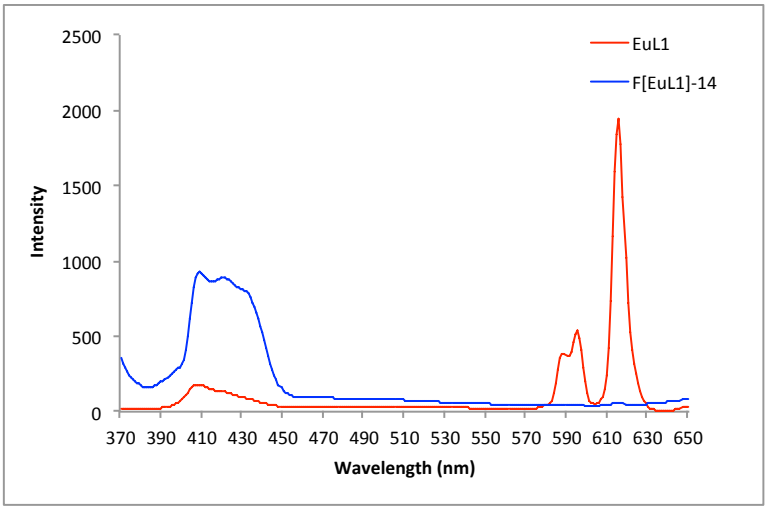

Figure 9. Emission spectra upon excitation at 360 nm of 1 mg/ml of Eu**L1** in dichloromethane (red line) and of F[Eu**L1**]-14 nanoparticles (blue line) in PBS pH 7,4

Discussion

The differences of size and melting temperature, between the nanoparticles containing the complexes and the empty ones, confirmed that the complexes have been encamped inside the PLGA NPs. Moreover, the presence of Lu(**L1**)$(NO_3)_3$ or Eu(**L1**)$(NO_3)_3$ gives rise to an increased thermal stability of the assembly. Despite this interesting result, the complexes inside the PLGA NPs lose their fluorescence ability: they are probably disassembled and the ligand is no longer able to transfer energy to the metal (this process strongly depends on the distance between ligand and metal). Indeed, when Eu(**L1**)$(NO_3)_3$ is dissolved alone in the solvent reaction it emits at 616 nm upon excitation at 360 nm as expected, while the complex inside the nanoparticles lost this ability; moreover, when in the reaction solvent PLGA [50:50] either [75:25] is added, no fluorescence signal is detected after more or less 15 minutes. Probably the hydroxyl groups interacting with the metal or the whole complex, breaking its structure: therefore the metal is not energized by the energy transfer and consequently does not emit a detectable signal. Nevertheless, PLGA does not completely shield from the surrounding aqueous environment, so the presence of water molecules inside the nanoparticles could lead to non-radiative quenching phenomena, as it is known the multi phonon relaxation in the case of Eu. Finally, the two complexes Lu(**L1**)$(NO_3)_3$ and Eu(L1)$(NO_3)_3$ are encapsulated inside [50:50] or [75:25] NPs losing their fluorescence emission.

rac-[Eu(L1)(tta)2(H2O)]$(NO_3)_3$ embedded in PLGA NPs

Size and Z-potential Characterization

Changing the ligand the fluorescence of the Eu(III) remains almost identical with slightly differences in intensity rather than the pattern of emission. Moreover, from the previous evidence of encampment, the complex has been synthesized keeping constant the concentration of PVA, the solvent (acetone 85% and ethanol 15%), the temperature at 37°C and the pH at 9. Only the concentration of *rac*-[Eu(**L1**)(tta)2(H2O)]$(NO_3)_3$ has been reduced to optimize the new system in terms of size and fluorescence. The decrease of concentration did not bring any benefit to the system and therefore the best formulations are such as with 1 mg for entering the compositions (F[Eu(**L1**)(tta)2(H2O)]-1 and F[Eu(**L1**)(tta)2(H2O)]-5). The synthesized nanoparticles were approximately 224,7 nm for [50:50] and 203,6 for [75:25] with an excellent emission intensity in PBS (table 6) and with a Z-potential of -2.3 mV and -4,67 mV respectively. Moreover, they were stable in PBS and Milli-Q water without any aggregation phenomena. So F[Eu(**L1**)(tta)2(H2O)]-1 and F[Eu(**L1**)(tta)2(H2O)]-5 NPs were investigated with AFM, DSC and Fluorometer.

Formulation.	PLGA (Mg/ml)	Complex (Mg/ml)	Z-a (nm)	PDI	St-dev (nm)	Emission Intensity (614 nm)
F[Eu(**L1**)(tta)2(H2O)]-1	[50:50] 10	1	224,7	0,1	66,2	8827,49
F[Eu(**L1**)(tta)2(H2O)]-2	[50:50] 10	0,5	231	0,064	66,8	458,39
F[Eu(**L1**)(tta)2(H2O)]-3	[50:50] 10	0,25	179,3	0,08	47,2	157,01
F[Eu(**L1**)(tta)2(H2O)]-4	[50:50] 10	0,01	178,8	0,05	47,8	-
F[Eu(**L1**)(tta)2(H2O)]-5	[75:25] 10	1	203,6	0.08	59,4	8852,69

Table 6. Formulations and DLS results (Z-average, PDI, st-deviation) of PLGA[Eu(**L1**)(tta)2(H2O)] nanoparticles synthesized by stirring.

Figure 10 shows an example of DLS diagram in which F[Eu(**L1**)(tta)$_2$(H$_2$O)]-5 NPs are mono- dispersed distributed around 160 nm with a standard deviation of 51,8 nm.

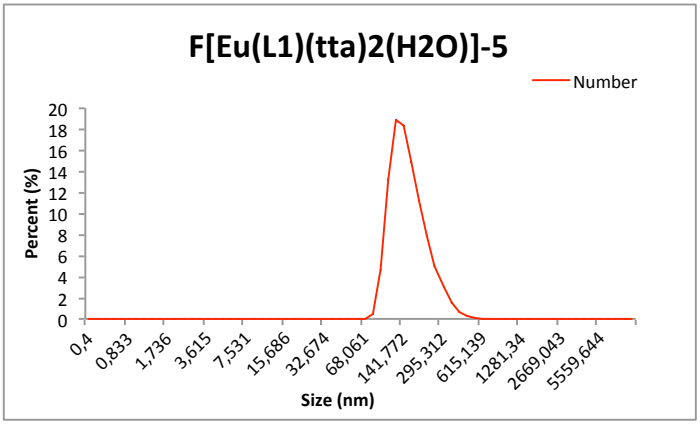

Figure 10. DLS diagram of F[Eu(**L1**)(tta)$_2$(H$_2$O)]-5 NPs dispersed in PBS. The size reported in table 7 is the average value calculated on three different samples.

AFM images reveal a strong aggregation mainly due to the preparation method used for the analyses. A statistical analysis was conducted with the GUI program and Gwyddion program to confirm the DLS data (table 7). A real result was not obtained for F[Eu(**L1**)(tta)$_2$(H$_2$O)]-1 with GUI program, however, the data obtained from the second statistic confirms the DLS data. Instead, for F[Eu(**L1**)(tta)$_2$(H$_2$O)]-5 similar results were obtained employing the two programs according to the Z-average. Therefore the subsequent analyses will be performed using only the Gwyddion program. Figure 11C shows *rac*-[Eu(**L1**)(tta)$_2$(H$_2$O)](NO$_3$)$_3$ embedded in [75:25] NPs with spherical shape and uniform distribution.

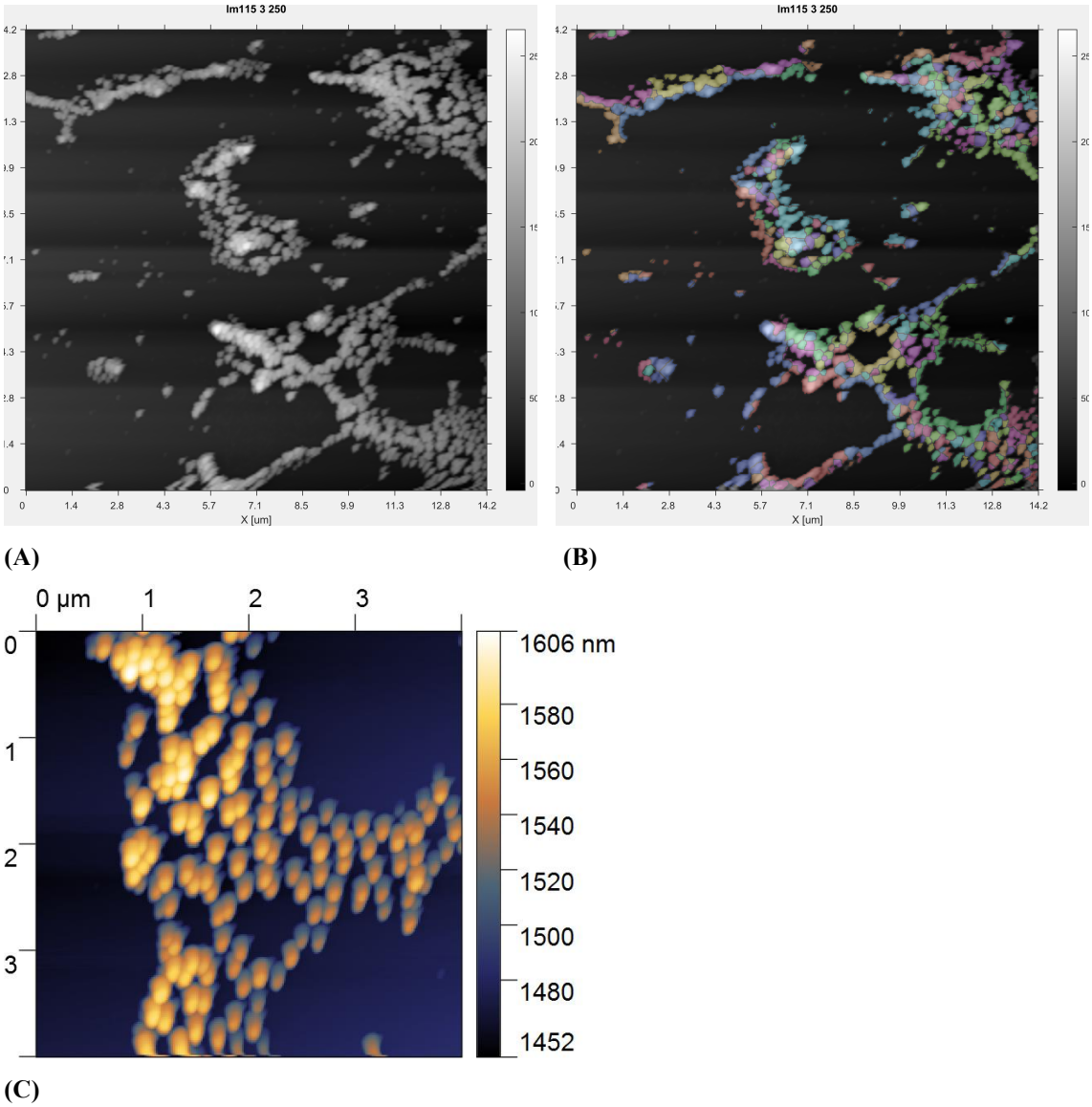

Figure 11. (A) AFM image of F[Eu(**L1**)(tta)$_2$(H$_2$O)]-5 NPs processed by GUI program; **(B)** application of Watershed algorithm; **(C)** AFM image of F[Eu(**L1**)(tta)$_2$(H$_2$O)]-5 NPs processed by Gwyddion program

Simple	Population	GUI statistic (nm)	Population	Gwyddion statistic (nm)	DLS size (nm)
F[Eu(**L1**)(tta)$_2$(H$_2$O)]-1	-	-	30	202,99 ± 33,45	224,7 ± 66,2
F[Eu(**L1**)(tta)$_2$(H$_2$O)]-5	103	202,5 ±	30	204,53 ± 29,49	203,6 ± 59,4

Table 7. Compare between DLS data and AFM statistics

Tm evaluation

Also in this case the calculation of the melting temperature of *rac*-[Eu(**L1**)(tta)$_2$(H$_2$O)](NO$_3$)$_3$ embedded in PLGA NPs has detected a variation of 4 degrees (34,02 ± 0,029 °C for [50:50] and 38,47 ± 0,064 °C for [75:25]) compared to the empty ones. Figure 12 shows the DLS diagram and the relative calculation of the tm.

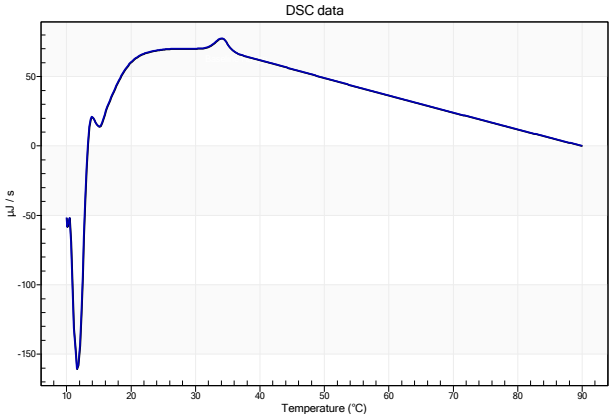

(A)

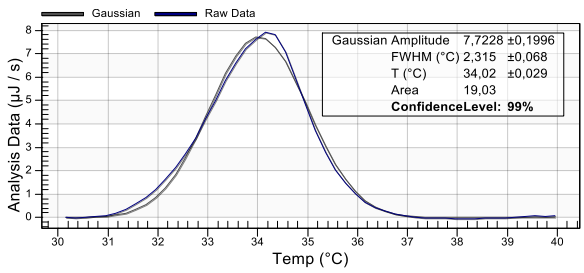

(B)

Figure 12. (A) DSC data of F[Eu(**L1**)(tta)$_2$(H$_2$O)]-5 NPs is visible a peak around the Tm point. **(B)** Calculation of Tm using Gaussian approximation with 99% of Confidence Level.

Fluorescence analysis

Upon excitation at 360 nm the complex in dichloromethane exhibited the usually high intensity emission around 616 nm relating to the $^5D_0$-$^7F_2$ transition and the weak ones around 578 and 590 nm relating to $^5D_0$-$^7F_0$ and $^5D_0$-$^7F_1$ [43, 45]. As described in table 7 nanoparticles containing the complex showed an emission slightly shifted towards 614 nm, this is probably due to the intricate environment around the metal (ligand, hydroxyl groups of PLGA, a small portion of water molecule, and so on). To measure the intensity, it was necessary to dilute the sample 5 times and set the instrument sensitivity to medium, since the samples showed high response. The following results were confirmed for both the PLGA variants. In figure 13 the emission spectra are reported for the same *rac*-[Eu(**L1**)(tta)2(H2O)]$(NO_3)_3$ embedded in [50:50] NPs dissolved by three different solvents: (A) PBS pH 7,4, (B) dichloromethane; (C) Milli-Q water. All of the three spectra show a high emission signal relating to Eu fluorescence pattern. The emission in water is less intense than in the other two cases, this is probably due to an enhanced multiphonon relaxation [49] than in the PBS where the presence of ions could slow down the entry of water inside the nanoparticles and increase the shielding from the external environment by PLGA. Moreover, in both spectra (A) and (C) there is another weak peak around 410 nm related to the ligand fluorescence. This suggests that a portion of the ligands does not transfer energy to the metal probably due to de-coordination worked by PLGA: indeed, the energy transfer depends strongly on the distance between the antenna and the acceptor. The dichloromethane is usually employed to destroy the nanostructure acting on the weak interaction that hold on the nanocarrier. Therefore the presence of emission in the spectrum (B) is due to the release of the complex in the solvent, which was contained inside the nanoparticles. Interestingly, the ligand fluorescence is not detected suggesting that it was bonding effectively to the metal. As can also be seen the empty nanoparticles do not give any considerable signal.

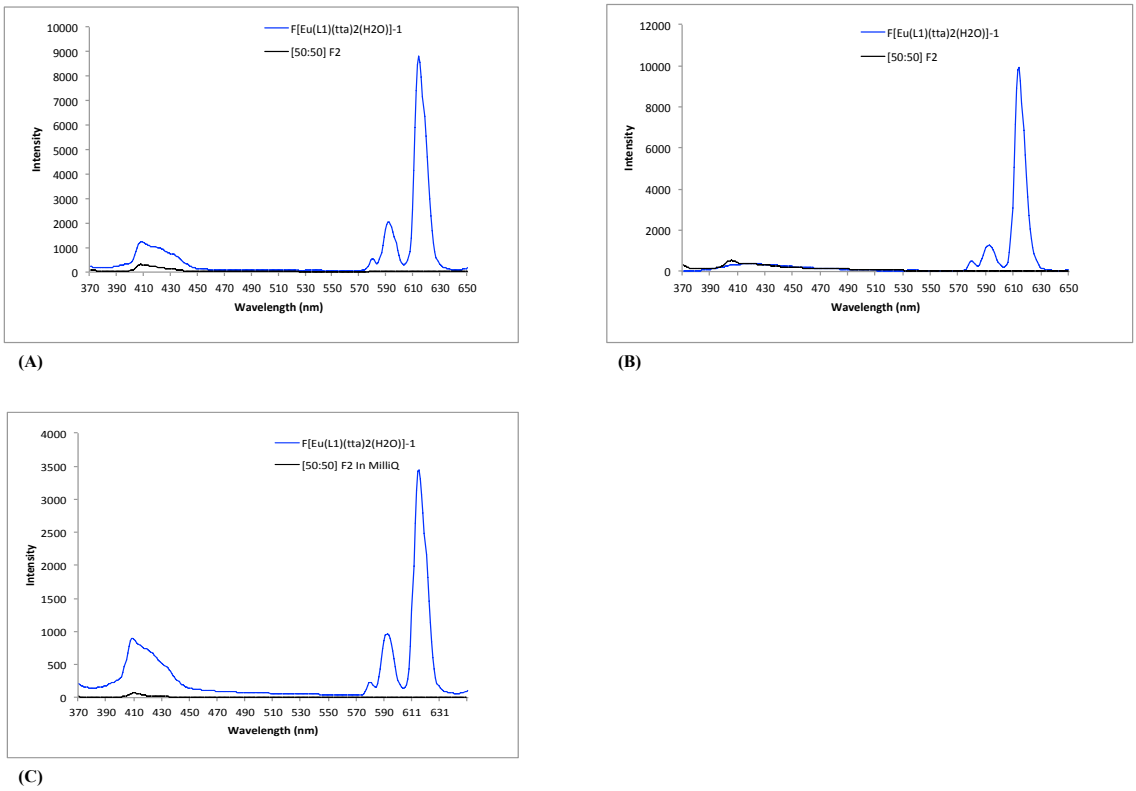

Figure 13. Spectra of *rac*-[Eu(**L1**)(tta)$_2$(H$_2$O)](NO$_3$)$_3$ embedded in [50:50] NPs (blue line) and empty ones (black line) dissolved by three different solvents: **(A)** PBS pH 7,4, **(B)** dichloromethane; **(C)** Milli-Q water.

Finally, the trend of the peak at 614 nm over time (24 hours) has been also studied to evaluate the fluorescence efficiency of the system at 20 °C and 37 °C (the working temperature in vitro either vivo studies). The points were collected at 0, 5, 10, 15, 30, 60, 120, 180, 360 and 1400 minutes (figure 14). At 37°C, initially the two formulations show the same trend and only after 120 minutes there is a greater stability of [75:25]. At the end of the analysis only the [75:25] still show a not indifferent signal. The cause of the signal increase at point 360 is not clear, perhaps it can be explained by the concentration quenching phenomena in which the increase in concentration of the complex (more concentrated inside the nanoparticles) is correlated with a lowering of the fluorescence signal. After 360 minutes a high amount of complex is released. The same behavior was also detected for [50:50] at the same point at 20°C. In figure 14B the loss in fluorescence capacity is less pronounced for both formulations, however [75:25] decays with a more evident linear trend compared to [50:50].

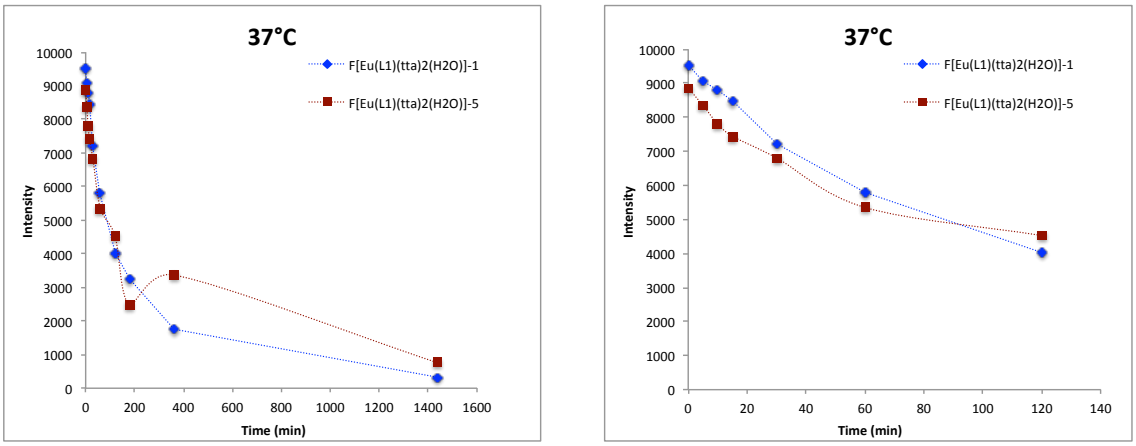

(A)

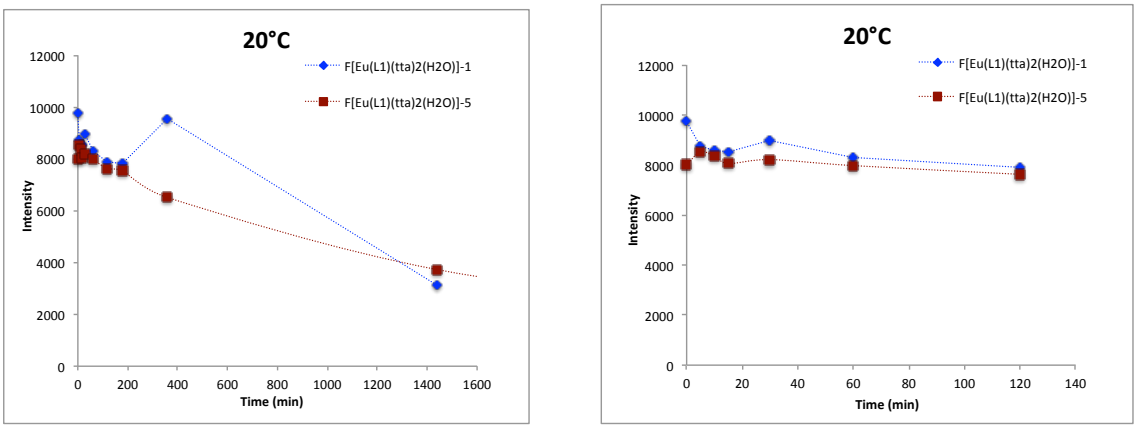

(B)

Figure 14. Radiative decay (peak at 614 nm) over time of the PLGA[F[Eu(**L1**)(tta)$_2$(H$_2$O)]-1] and PLGA[F[Eu(**L1**)(tta)$_2$(H$_2$O)]-1] nanoparticles at 20°C **(A)** and 37°C **(B)**; points collected at 0, 5, 10, 15, 30, 60, 120, 180, 360 and 1400 minutes)

Discussion

rac-[Eu(**L1**)(tta)2(H2O)]$(NO_3)_3$ has been successfully encapsulated preserving its fluorescence ability in PBS pH 7,4 and Milli-Q water and at the same time obtaining nanoparticles of interesting size for in vitro or in vivo applications. As already verified for the empty nanoparticles the watershed algorithm fails to correctly identify the single nanoparticles. Nevertheless Gwyddion statistic confirms the DLS data. Since for F[Eu(**L1**)(tta)2(H2O)]-5 similar results were obtained employing the two programs according to the Z-average, the subsequent analyses will be performed using only the Gwyddion program. The increase in melting temperatures for both formulations compared to empty nanoparticles suggests a stabilizing effect of the encapsulated complex. It certainly plays a role in the nanostructure assembly. This was already detected by encamping Eu(**L1**)$(NO_3)_3$ and Lu(**L1**)$(NO_3)_3$. The emission spectra in dichloromethane suggests further the efficient encapsulating of PLGA. The temperature influences negatively the radiative decays accelerating the release of the complex to 37 degrees. *rac*-[Eu(**L1**)(tta)2(H2O)]$(NO_3)_3$ in aqueous environment does not emit due to quenching phenomena and de-coordination acting by water molecules which compromise the effectiveness of sensitizing. The study carried out at 37°C suggests that the system based on [75:25] is more stable than [50:50] according to the different melting temperatures; while there is no substantial decay trends at 20°C. The success of this test probably lies in the different number of coordination (8) with respect to the previous complexes Eu(**L1**)$(NO_3)_3$ and Lu(**L1**)$(NO_3)_3$ (4), so the complex *rac*-[Eu(**L1**)(tta)2(H2O)]$(NO_3)_3$ would be able to more effectively preserve from decomplextation (acting by PLGA and water molecules) and better isolate the metal from the intricate environment.

rac-[Eu(L2)(tta)2(H2O)]CF3SO$_3$ and EuL3 embedded in PLGA NPs

Size and Z-potential Characterization

As described previously, changing the ligand the fluorescence of the Eu(III) remains almost identical with slightly differences in intensity rather than the pattern of emission. Moreover, from the study evidence of rac-[Eu(**L1**)(tta)2(H2O)](NO$_3$)$_3$ encampment, the nanoparticles has been synthesized keeping constant the concentration of PVA, the solvent (acetone 85% and ethanol 15%), the temperature at 37°C, the pH at 9 and with 1 mg of complex (table 8). The synthesized nanoparticles were approximately 223 nm for [50:50] and 221,7 nm for [75:25] with excellent emission intensity in PBS pH 7,4 and Z-potential of -2,67 mV and -5,14 mV. Similar results have been obtained for nanoparticles containing [Eu(**L1**)(tta)2(H2O)](NO$_3$)$_3$. To further reduce the size, the same synthesis was carried out using emulsification sonication. . The dimensions were reduced to 183,7 nm for [50:50] and 203,7 for [75:25] maintaining high emission with Z-potential of -5,37 mV and -4,51 mV (table 9). Also Eu**L3** was embedded in [50:50] nanoparticles with the same sonication method (size around 175 nm with – 4,51 mV as Z-potential). S[Eu(**L2**)(tta)2(H2O)]-1 and S[Eu(**L2**)(tta)2(H2O)]-2 NPs were investigated with AFM, DSC and Fluorometer while only the fluorescence was studied for Eu**L3** nanoparticles.

Formulations	PLGA (Mg/ml)	Z-a (nm)	PDI	St-dev (nm)
F[Eu(**L2**)(tta)2(H2O)]-1	[50:50] 10	223	0,114	71,6
F[Eu(**L2**)(tta)2(H2O)]-2	[75:25] 10	221,7	0,053	58,29

Table 8. Formulations and DLS results (Z-average, PDI, st-deviation) of PLGA[Eu(**L2**)(tta)2(H2O)] nanoparticles synthesized by stirring.

Formulations	PLGA (Mg/ml)	Z-a (nm)	PDI	St-dev (nm)	Emission Intensity (615 nm)
S[Eu(**L2**)(tta)$_2$(H$_2$O)]-1	[50:50] 10	183,7	0,105	52,07	7000
S[Eu(**L2**)(tta)$_2$(H$_2$O)]-2	[75:25] 10	203,7	0,139	54,26	7880

Table 9. Formulations and DLS results (Z-average, PDI, st-deviation) of PLGA[Eu(**L2**)(tta)$_2$(H$_2$O)] nanoparticles synthesized by sonication.

Figure 15 shows an example of DLS diagram in which S[Eu(**L2**)(tta)$_2$(H$_2$O)]-1 NPs are mono- dispersed distributed around 141 nm with a standard deviation of 52,07 nm.

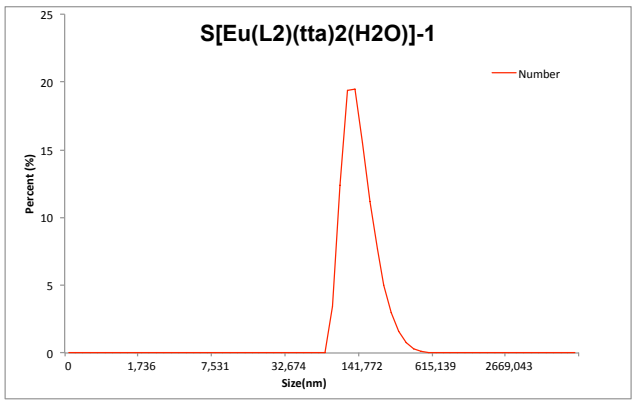

Figure 15. DLS diagram of S[Eu(**L2**)(tta)$_2$(H$_2$O)]-1 NPs dispersed in PBS. The size reported in table 10 is the average value calculated on three different samples.

The AFM image (figure 16) reveals single nanoparticles [50:50] with spherical shape distributed around 183 nm as expected; indeed, the statistical analysis confirms the Z-average detected for both the samples (table 10).

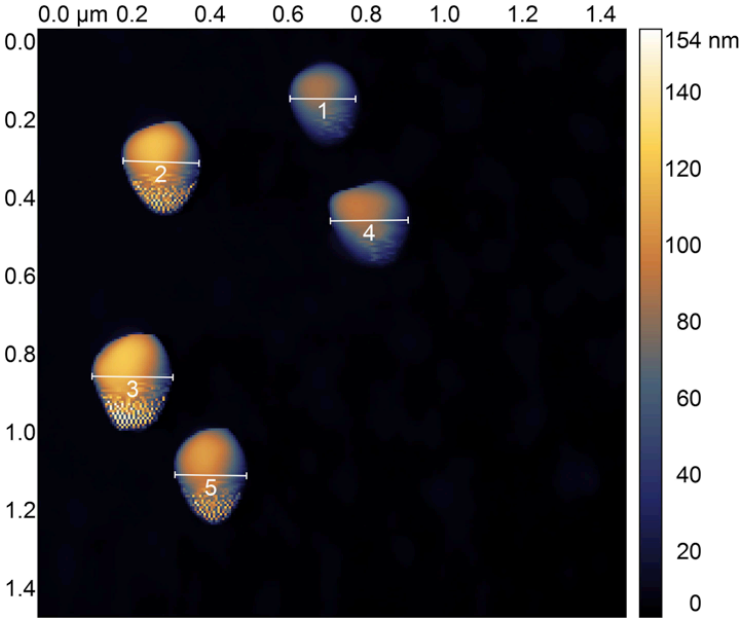

Number	Size (nm)
1	170
2	195
3	207
4	199
5	183

Figure 16. AFM image of S[Eu(**L2**)(tta)$_2$(H$_2$O)]-1] NPs processed by Gwyddion program with relative size measure

Simple	Population	Gwyddion statistic (nm)	DLS size (nm)
S[Eu(**L2**)(tta)$_2$(H$_2$O)]-1	30	180 ± 26	183,7 ± 52,07
S[Eu(**L2**)(tta)$_2$(H$_2$O)]-2	30	195,3 ± 40	203,7 ± 54,26

Table 10. Comparison between DLS data and AFM statistics

Tm evaluation

Also in this case the calculation of the melting temperature of *rac*-[Eu(**L2**)(tta)2(H2O)]$(NO_3)_3$ embedded in PLGA NPs has detected a variation of 4 degrees (33,5 ± 0,05 °C for [50:50] and 38 ± 0,089 °C for [75:25]) compared to the empty ones. Figure 17 shows the shift of the Tm point between the two PLGA compositions containing the complex and an example of calculation of melting point.

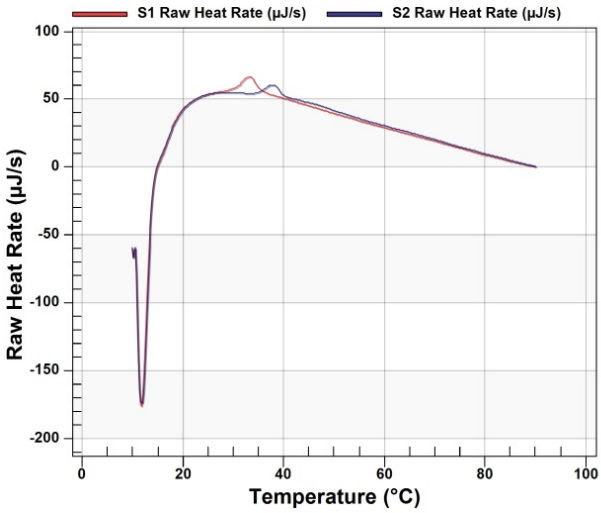

(A)

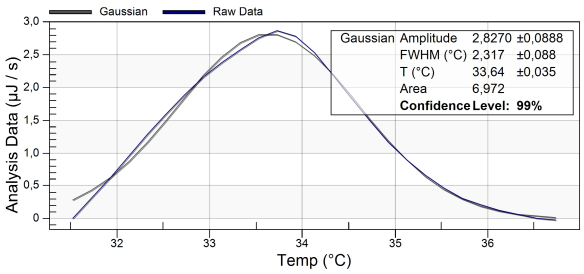

(B)

Figure 17. Superimposition of DSC diagram for S1 ([Eu(**L2**)$(tta)_2(H_2O)$]·CF_3SO_3 complex embedded in [50:50] , red line) and S2 ([Eu(**L2**)$(tta)_2(H_2O)$]·CF_3SO_3 complex embedded in [75:25],blue line) **(A)** ; calculation of Tm of S[Eu(**L2**)$(tta)_2(H_2O)$]-1 NPs **(B)**

Fluorescence analysis

The excitation wave was shifted to 350 nanometres, without modifying Eu(III) emission pattern, since the fluorescence response of *rac*-[Eu(**L2**)(tta)$_2$(H$_2$O)]·CF$_3$SO$_3$ was greater at this wavelength [45]. As described in table 9 nanoparticles containing the complex show an emission slightly shifted towards 615 nm than the usual 616 nm of Eu(III), this is probably due to the intricate environment around the metal (ligand, hydroxyl groups of PLGA, a small portion of water molecule, and so on). To measure the intensity, it was necessary to dilute the sample 10 times and selection medium as sensitivity, since the samples showed high response. In figure 18 the emission and excitation spectra are reported for the same *rac*-[Eu(**L2**)(tta)$_2$(H$_2$O)]·CF$_3$SO$_3$ embedded in [75:25] NPs dissolved in PBS pH 7,4 (A) and dichloromethane (B). The excitation spectra recorded for the nanoparticles containing [Eu(**L2**)(tta)$_2$(H$_2$O)]·CF$_3$SO$_3$ complex are identical and superimposable with the excitation spectra of the complex alone [45]. The presence of two excitation bands around 280 nm and 350 nm respectively is a clear indication of a ligand to metal energy transfer from both ligands (**L1** and tta). Since the dichloromethane enhance realise of the complex inside the nanoparticles, the presence of excitation and emission spectra detected in dichloromethane (B) suggests that the complex was substantially undamaged inside the nanocarrier. Moreover, in figure 19 A, [75:25] NPs show more intense emission fluorescence than the [50:50] ones. Furthermore, a weak emission band around 400 nm due to the fluorescence of the ligand is also visible greater in S[Eu(**L2**)(tta)2(H2O)]-1 NPs than S[Eu(**L2**)(tta)2(H2O)]-2, suggesting that the antenna effect loses more effectiveness in [50:50].

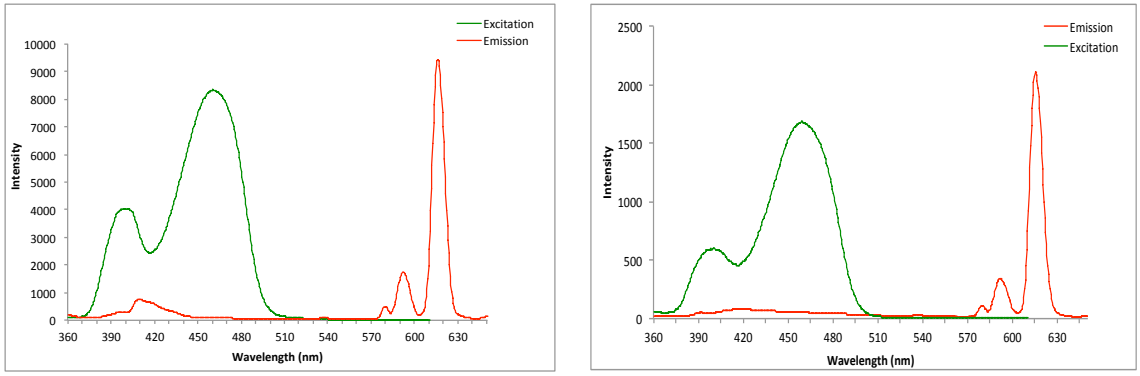

(A) **(B)**

Figure 18. Excitation (green line) and emission (red line) spectra of *rac*-[Eu(**L2**)(tta)$_2$(H$_2$O)]·CF$_3$SO$_3$ embedded in [75:25] NPs dissolved in **(A)** PBS pH 7,4 and **(B)** dichloromethane

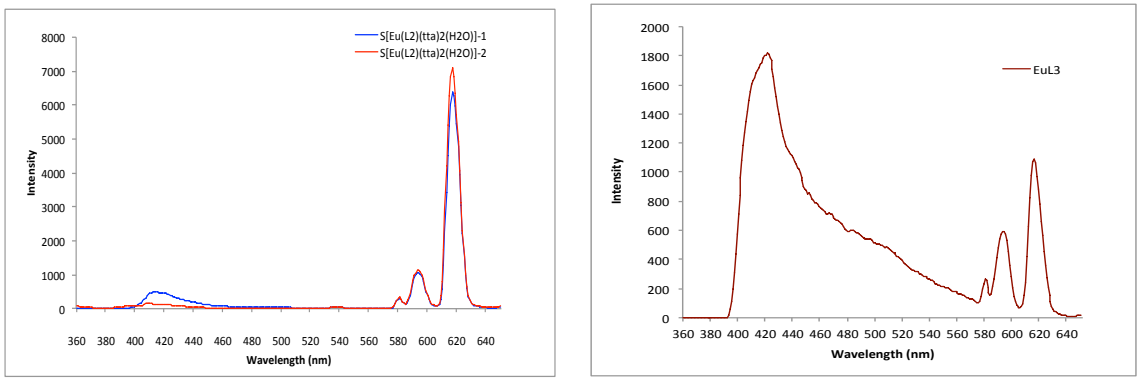

(A) **(B)**

Figure 19. (A) Superposition of emission spectra of *rac*-[Eu(**L2**)(tta)$_2$(H$_2$O)]·CF$_3$SO$_3$ embedded in [50:50] NPs (blue line) and [75:25] NPs (red line); **(B)** emission spectra of Eu**L3** embedded in [50:50] NPs dissolved in PBS pH 7,4.

When Eu**L3** is embedded in the PLGA nanoparticles, upon excitation in the ligand absorption band (320 nm), very low luminescence intensity is detected (figure 19 B) and the emission band around 420 nm, due to the quinoline fluorescence [43] dominates the spectrum. This suggests an ineffective incorporation of Eu**L3** in the polymer in agreement with the small size detected similar to the empty nanoparticles. Moreover, the small amount of the embedded complex undergoes structural changes, which negatively affect the efficiency of ligand to metal energy transfer.

The total quantum yield (ϕ_{Tot}), that is defined by the number of photons emitted by the lanthanide ion/number of photons absorbed by the ligand has been estimated for [Eu(**L2**)(tta)$_2$(H$_2$O)]·CF$_3$SO$_3$ complex embedded in 50:50 and 75:25 PLGA NP's. Both systems show a good ϕ_{Tot} value (20% for the former, 25% for the latter). The slightly higher ϕ_{Tot} recorded for the complex embedded in the 75:25 PLGA composition is consistent with the lower intensity of the emission band attributable to the ligand fluorescence than in the case of PLGA 50:50.

The trend of the peak at 615 nm has been also studied over time (24 hours) to evaluate the fluorescence efficiency of the system at 20 °C and 37 °C (the working temperature in vitro either vivo studies). The points were collected at 0, 5, 10, 15, 30, 60, 120, 180, 360 and 1400 minutes (figure 18). At 20°C the emission intensity decrease in the same way for both PLGA compositions while at 37°C the emission intensity decrease faster for [50:50] NPs. This phenomenon, related to the breaking of the PLGA assembly and the release of the complex in solution, is more significant at higher temperatures (37°C), in particular in the case of PLGA 50:50, whose melting temperature (33°C) is significantly lower than the working one (37°C). Moreover, the evolution over time of excitation spectrum of [75:25] at 37°C decreases according to the fluorescence decay as expected (figure 21).

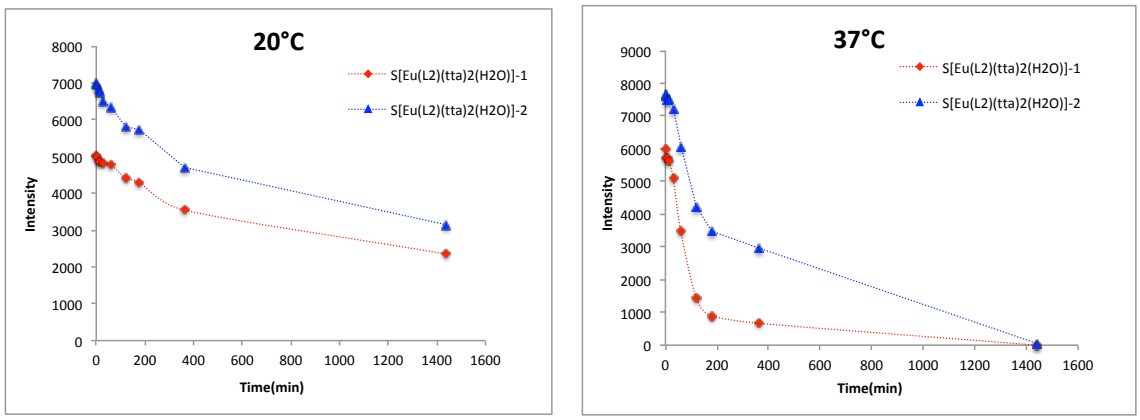

(A) (B)

Figure 20. Radiative decay (peak at 615 nm) over time of the PLGA[S[Eu(**L2**)(tta)$_2$(H$_2$O)]-1] and PLGA[S[Eu(**L2**)(tta)$_2$(H$_2$O)]-2] nanoparticles at 20°C **(A)** and 37°C **(B)**; points collected at 0, 5, 10, 15, 30, 60, 120, 180, 360 and 1400 minutes.

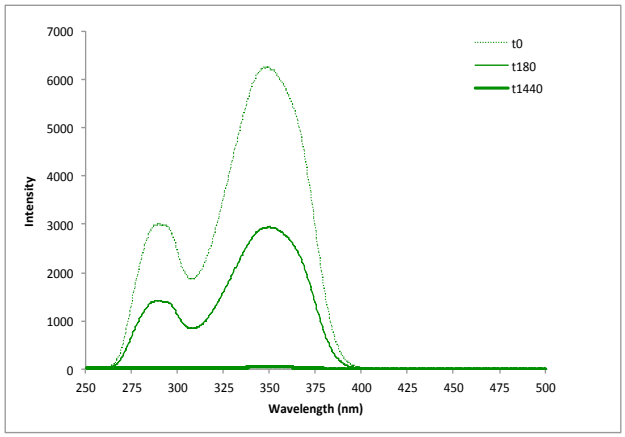

Figure 21. Excitation spectra of [Eu(**L2**)(tta)$_2$(H$_2$O)]·CF$_3$SO$_3$ embedded in [75:25] NPs at 37°C collected at time 0, 180, 360 minutes

In contrast to the case of [Eu(**L2**)(tta)$_2$(H$_2$O)]·CF$_3$SO$_3$ complex dissolved in organic solvents such as acetonitrile or methanol [45] the decay profiles of its assembly with PLGA cannot be fitted by a single exponential function. In these cases, the best estimation of the excited state lifetime is given by the 1/e folding time, which decrease over the time at 37°C (0.55 ms, t=0; 0.48 ms, t=3h and 0.37 ms, t=24h for the 75:25 formulation, figure 22 A). The decay time for the Eu(III) complex embedded in PLGA 50:50 is similar at t=0 (0.52 ms) but decreases quickly over the time (0.40 ms, t=3h and 0.30 ms, t=24h; figure 22 B). The observed shortening of the Eu(III) lifetime is probably due to the activation of non-radiative mechanism able to quench the $^5D_0$ Eu(III) excited state. As described for [Eu(**L2**)(tta)$_2$(H$_2$O)](NO$_3$)$_3$, the breaking of the PLGA assembly allows water molecules to have access to the metal and activate the well-known non-radiative multiphonon relaxation process [49]. Further the hydroxyl groups of PLGA could also interact with the metal de-coordinating the whole complex. These two phenomena have not indifferent role in the decrease of fluorescence compromising the sensitizing process.

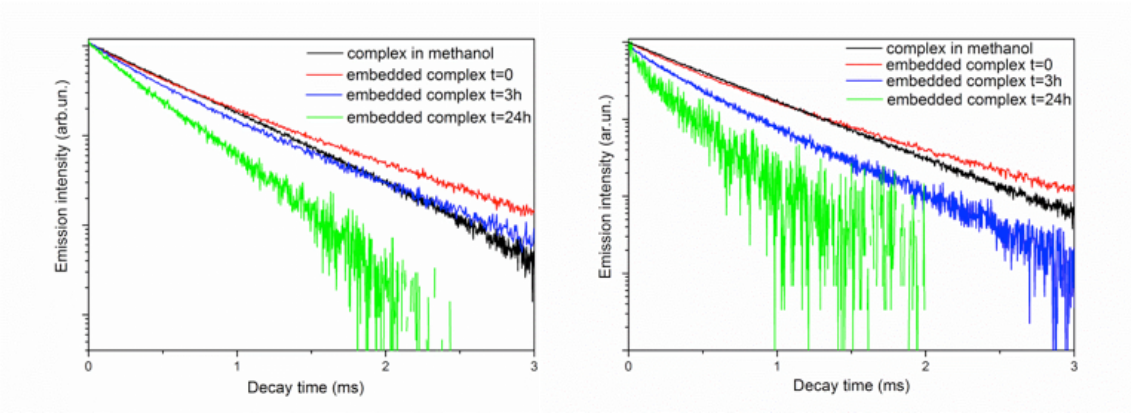

(A) **(B)**

Figure 22. Evolution of the decay curves of the $^5D_0$ excited state of Eu(III) over the time (0→24 h) for [Eu(**L2**)(tta)$_2$(H$_2$O)]·CF$_3$SO$_3$ complex embedded in **(A)** PLGA 75:25 at 37°C, in phosphate buffer aqueous solution (excitation 350 nm; emission 615 nm); **(B)** PLGA 50:50 at 37°C, in phosphate buffer aqueous solution (excitation 350 nm; emission 615 nm). The decay curve of the complex in methanol is also reported as a reference [45].

Discussion

In the case of [Eu(**L2**)(tta)$_2$(H$_2$O)]·CF$_3$SO$_3$ the simple-emulsion method conducted under sonication not only allowed to further reduce the size, but also to obtain a system with a high fluorescence intensity, while Eu**L3** was not efficiently incorporated into the polymer probably due to its hydrophilic characteristic. Indeed, it is well known that the present PLGA formulations are suitable for embedding hydrophobic rather than hydrophilic complexes. Again the presence of the complex brings to a greater thermal stability of the system, a characteristic that is valued in the fluorescence evolution over the time. In particular [75:25] it is able to preserve more effectively the emission capacity of the complex even at 37°C, interestingly in view of possible in vivo or in vitro studies. Moreover the good value of quantum yield make PLGA Nps containing [Eu(**L2**)(tta)$_2$(H$_2$O)]·CF$_3$SO$_3$ interesting for optical imaging applications, indeed the quantum yield of many lanthanide and d-block compounds used for cellular imaging is in the 4-10% range [47]. Finally, It is interesting to note that the sensitization of the Eu(III) luminescence can be achieved upon excitation in a wide UV spectral range (250-400 nm). Potentially, this gives the opportunity to choose the more suitable excitation wavelength. In particular, the excitation peak around 350 (in the N−UV region) is particularly attractive for biomedical application since this wavelength is hardly absorbed by interfering biomolecules necessarily present in a real matrix.

rac-[Y(L2)(tta)$_2$(H$_2$O)]CF$_3$SO$_3$ embedded in PLGA NPs

Size and Z-Potential Characterization

Since the NMR and elemental analysis data show that *rac*-[Y(**L2**)(tta)$_2$(H$_2$O)]CF$_3$SO$_3$ has not only been correctly synthesized but also has the same structure as the *rac*-[Eu(**L2**)(tta)$_2$(H$_2$O)]CF$_3$SO$_3$; previous sonication protocols have been used for the formation of nanoparticles for the two compositions. Table 11 shows slightly differences in size between [50:50] and [75:25]; nevertheless the nanoparticles were stable in PBS at pH 7,4 and in water suspension. Figure 23 shows a mono-dispersed distribution of [50:50] NPs.

Formulations	PLGA (Mg/ml)	Z-a (nm)	PDI	St-dev (nm)
S[Y(**L2**)(tta)$_2$(H$_2$O)]-1	[50:50] 10	199,6	0,15	54,2
S[Y(**L2**)(tta)$_2$(H$_2$O)]-2	[75:25] 10	219	0,162	62,57

Table 11. Formulations and DLS results (Z-average, PDI, st-deviation) of PLGA[Y(**L2**)(tta)$_2$(H$_2$O)] nanoparticles synthesized by sonication

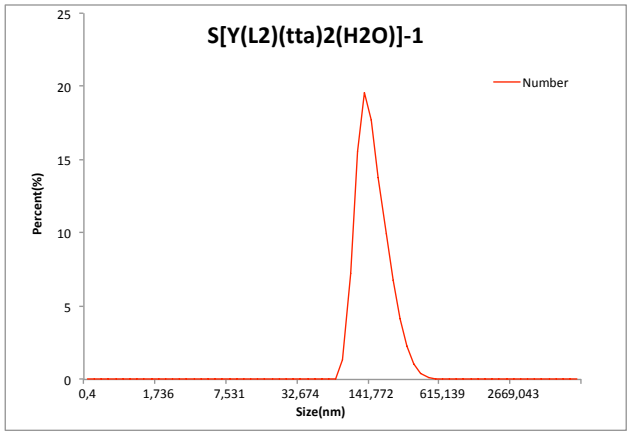

Figure 23. DLS diagram of S[Y(**L2**)(tta)$_2$(H$_2$O)] -1 NPs dispersed in PBS. The size reported in table 8 is the average value calculated on three different samples.

Also for this complex the AFM data are in agreement to DLS ones (table 12), moreover figure 24 shows nanoparticles of spherical shape.

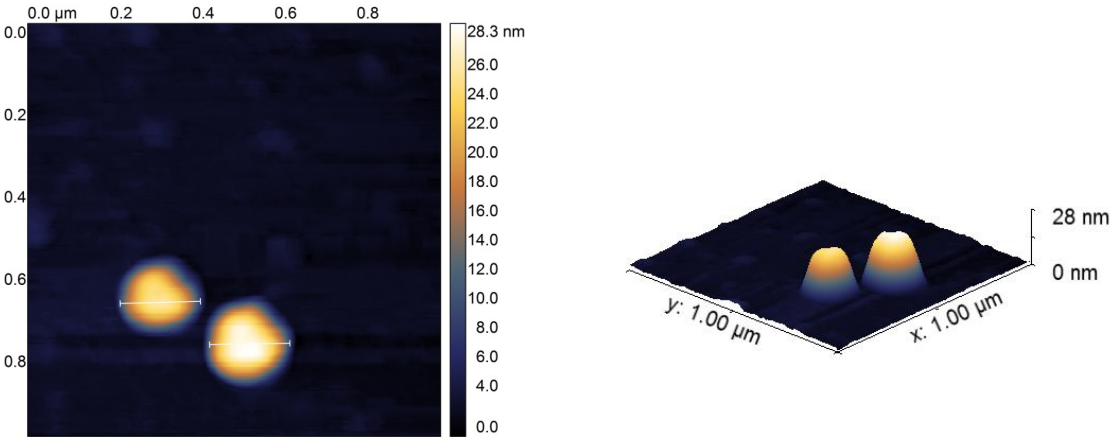

Figure 24. AFM images of [Y(**L2**)(tta)$_2$(H$_2$O)]·CF$_3$SO$_3$ complex embedded in PLGA 75:25

Simple	Population	Gwyddion statistic (nm)	DLS size (nm)
S[Y(**L2**)(tta)2(H2O)]-4	30	182,8 ± 32	199,6 ± 54,2
S[Y(**L2**)(tta)2(H2O)]-5	30	194,5 ± 34	219 ± 62,7

Table 12. Compare between DLS data and AFM statistics

Tm evaluation

No difference was noted in the melting temperature calculation of [50:50], again nanoparticles containing the complex show an increase of 4 degrees in the melting temperature (33,1 ± 0,07 °C) and compared to the empty ones while for [75:25] NPs the increase was slightly lower than the usual one (37,1 ± 0,05°C). Figure 25 shows a superimposition between PLGA[S[Eu(**L2**)(tta)2(H2O)]-1] and PLGA[S[Y(**L2**)(tta)2(H2O)]-4)] in which the two curves perfectly overlap at the tm point as expected since the coordination sphere is the same for both the complexes.

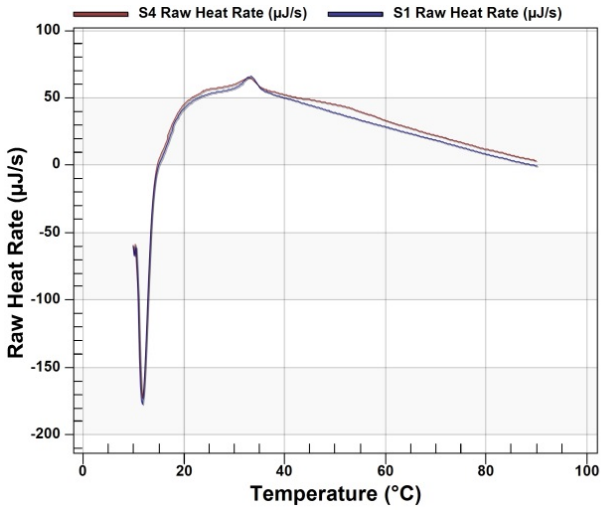

(A)

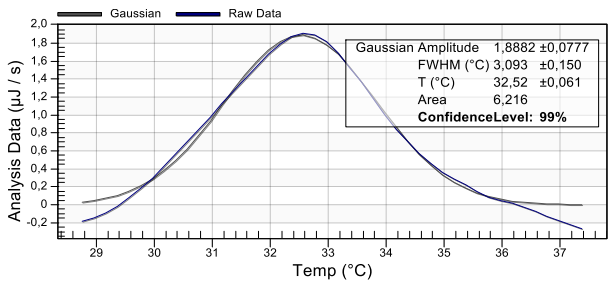

(B)

Figure 25. (A) Superimposition of DSC diagram for S1 ((Eu(**L2**)$(tta)_2(H_2O)]\cdot CF_3SO_3$ complex embedded in PLGA 75:25, blue line), and S4 (Y(**L2**)$(tta)_2(H_2O)]\cdot CF_3SO_3$ complex embedded in PLGA 50:50); **(B)** Calculation of melting temperature.

Fluorescence analysis

Yttrium does not emit upon excitation of the 350 nm of the ligand, so in the emission spectra it is detected only the ligand emission (figure 26).

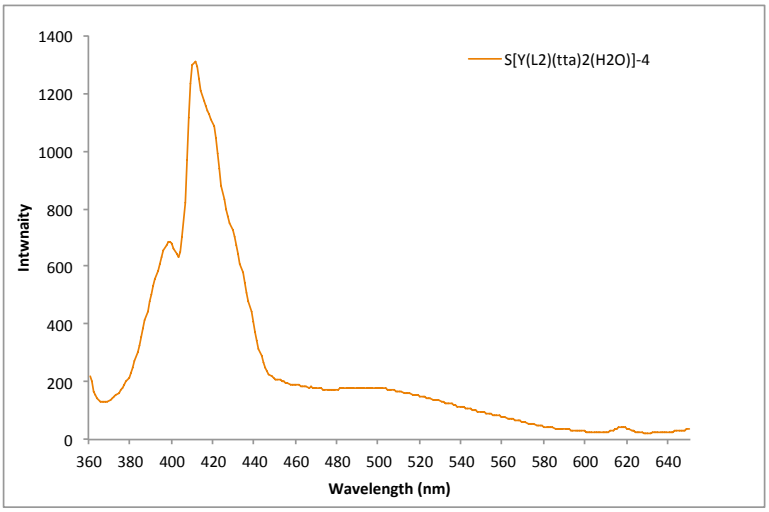

Figure 26. Emission spectra of $[Y(L2)(tta)_2(H_2O)]CF3SO_3$ embedded in [50:50] NPs

Discussion

Since the coordination sphere is the same for both metals (Y and Eu) the data have been the expected ones, although a little difference is present for [75:25] composition in size and Tm. This is probably due to the electronic difference between the two species of metal. Moreover the superimposition of DSC curves confirms that the Y and Eu have similar structure. *So rac*-[Y(**L2**)(tta)2(H2O)]CF3SO$_3$ has been effectively encamped as shown by the DLS data and the melting temperature data, in fact the presence of the complex (consideration verified for all the others) leads to greater thermal stability for both composition. Despite the non-fluorescence activity of Yttrium, it was possible to verify the emission of the ligand that suggests that the complex is definitely inside the nanoparticles. This system becomes interesting for possible imaging applications changing Y with its counterpart radiative (^{90}Y) able to give a signal for PET imaging.

Conclusion

All the complexes have been encamped inside the PLGA nanoparticles as demonstrated by the results of the calculation of the tm; indeed, for different complexes the same increase of 4 degrees occurred for the two compositions. This confirms the theory that the presence of the complexes inside the nanoparticles provides greater thermal stability. Moreover, it has been shown that the more hydrophobic lanthanide complexes are better encamped by the PLGA, which plays an important role in the de-coordination of the metal-ligand complex: indeed, Lu(**L1**)$(NO_3)_3$ or Eu(**L1**)$(NO_3)_3$ embedded inside PLGA does not emit due to a possible de-coordination exposing the metal to the water molecules with consequent quenching phenomena. On the other hand, the complex *rac*-[Eu(**L1**)(tta)2(H2O)]$(NO_3)_3$ inside the nanoparticles efficiently preserves the emission of the metal over time even at 37 °C. In other words, the greater coordination number 8 of *rac*-[Eu(**L1**)(tta)2(H2O)]$(NO_3)_3$ binds the metal more strongly, resisting to de-coordination more effectively than Lu(**L1**)$(NO_3)_3$ or Eu(L1)$(NO_3)_3$ (coordination number 4). In the case of PLGA [75:25] containing the complexes it shows greater thermal stability with a consequent slowly release at 37°C; this is an interesting feature for bio imaging studies. Finally, *rac*-[Eu(**L2**)(tta)2(H2O)]CF_3SO embedded in PLGA NPs represents a potential optical imaging agent for in vitro or in vivo testing, thanks to the small nanoparticles size (below 200 nm), the high emission intensity and quantum yield. Moreover, the PLGA is also capable to embed the analogous complex *rac*-[Y(**L2**)(tta)2(H2O)]CF_3SO_3, opening the way to design a nano-sized PET-imaging agent based on PLGA and ^{90}Y.

References

1. F. Danhier, E. Ansorena, J. M. Silva, R. Coco, A. Le Breton, V. Préat Journal of Controlled Release 2012, 161, 505–522.
2. Jain RA. The manufacturing techniques of various drug loaded biodegradable poly(lactide-coglycolide) (PLGA) devices. Biomaterials. 2000; 21:2475–2490.
3. Ruhe PQ, Hedberg EL, Padron NT, Spauwen PH, Jansen JA, Mikos AG. rhBMP-2 release from injectable poly (DL-lactic-co-glycolic acid)/calcium-phosphate cement composites. J Bone Jt Surg 2003; 85:75–81
4. Bala, I., Haribaran, S., and Kumar, R., PLGA nanoparticles in drug delivery: The state of the art. Critical Reviews in therapeutic Drug Carrier Systems, 21, 387-422 (2004).
5. Anderson, J.M., Shive, M.S., Biodegradation and biocompatibility of PLA and PLGA microspheres. Advanced Drug Delivery Reviews, 28, 5-24 (1997).
6. Alexis, F., Factors affecting the degradation and drug-release mechanism poly(lactide acid and poly(lactic acid-co-glycolic acid). Polymer International, 54-36-2015
7. D. Quintanar-Guerrero, E. Allemann, H. Fessi, and E. Doelker, Preparation technique and mechanism of formation of biodegradable nanoparticles from preformed polymers. Drug Development and industrial Pharmacy, 24(12), 1113-1128 (1998).
8. Kulkarni, S. A.; Feng, S.-S. Effects of Particle Size and Surface Modification on Cellular Uptake and Biodistribution of Polymeric Nanoparticles for Drug Delivery. Pharm. Res. 2013, 30, 2512–2522
9. Choi, H. S.; Liu, W.; Misra, P.; Tanaka, E.; Zimmer, J. P.; Ipe, B. I.; Bawendi, M. G.; Frangioni, J. V. Renal Clearance of Nanoparticles. Nat. Biotechnol. 2007, 25, 1165–1170.
10. McCall, R.L., Sirianni, R.W. PLGA Nanoparticles Formed by Single- or Double-emulsion with Vitamin E-TPGS. J. Vis. Exp. (82), e51015, doi:10.3791/51015 (2013).

11. Dinarvand R, Sepehri N, Manoochehri S, Rouhani H, Atyabi F: Polylactide-co-glycolide nanoparticles for controlled delivery of anticancer agents. Int J Nanomedicine 2011, 6:877.
12. Maeda H, Wu J, Sawa T, et al. Tumor vascular permeability and the EPR effect in macromolecular therapeutics: A review. J ControlRelease 2000;65:271– 84.
13. Petra Kocbek, *et al.* Targeting cancer cells using PLGA nanoparticles surface modified with monoclonal antibody. Journal of Controlled Release 120 (2007) 18–26
14. F. Danhier, E. Ansorena, J. M. Silva, R. Coco, A. Le Breton, V. Préat Journal of Controlled Release 2012, 161, 505–522.
15. M.L. Hans, A.M. Lowman Curr. Opin. Solid State Mater. Sci. 2002, 6, 319–327
16. Kirpotin DB, Drummond DC, Shao Y, *et al.* Antibody targeting of long-circulating lipidic nanoparticles does not increase tumor localization but does increase internalization in animal models. Cancer Res 2006;66:6732– 40
17. Gref R, Luck M, Quellec P, et al. "Stealth" corona-core nanoparticlessurface modified by polyethylene glycol (PEG): Influences of the corona (PEG chain length and surface density) and of the core composition on phagocytic uptake and plasma protein adsorption. Colloids Surf B Biointerfaces 2000;18:301–13.
18. Owens DE III, Peppas NA. Opsonization, biodistribution, and pharmacokineticsof polymeric nanoparticles. Int J Pharmacol 2006;307:93–102.
19. Sun Hwa Kim, Ji Hoon Jeong, *et al.* Target-Specific Cellular Uptake of PLGA Nanoparticles Coated with Poly(L-lysine)-Poly(ethylene glycol)-Folate Conjugate. Langmuir 2005, 21, 8852-8857
20. Kost J, Langer R. Responsive polymeric delivery systems. Adv Drug Deliv Rev 2001;46:125– 48.
21. Yin X, Hoffman AS, Stayton PS. Poly(N-isopropylacrylamide-copropylacrylic acid) copolymers that respond sharply to temperature and pH. Biomacromolecules 2006;7:1381–5.
22. Brown LR, Edelman ER, Fischel-Ghodsian F, et al. Characterization of glucose-mediated insulin release from implantable polymers. J Pharmacol Sci 1996;85:1341–5.

23. S. Naik, E. E. Carpenter J. of Appl. Phis. 2008, 103, 07A313
24. J. Hu, J. Guo, Z. Xie, D. Shan, E. Gerhard, G. Qian, J. Yang Acta Biomaterialia 2016, 29, 307–319.
25. C. Fornaguera, N. Feiner-Gracia, G. Calderó, M.J. García-Celmac, C. Solans Colloids and Surfaces B: Biointerfaces 2016, 147, 201–209.
26. T. Betancourt, K. Shah, L. Brannon-Peppas J Mater Sci: Mater Med 2009, 20; 387–395.
27. P. P. Wyss, L. C. Herrera, N. S. Bouteghmes, M. Sarem, W. Reichardt, J. Leupold, J. Hennig, V. P. Shastri ACS Omega 2016, 1, 182−192.
28. L. J. Cruz, I. Que, M. Aswendt, Alan Chan, M. Hoehn, C. Löwik Nano Res. 2016, 9(5), 1276–1289.
29. P. Zhao, M. Zheng, C. Yue, Z. Luo, P. Gong, G. Gao, Z. Sheng, C. Zheng, L.Cai Biomaterials 2014, 35, 6037-6046.
30. B. Zheng, Y. Bai, H. Chen, H. Pan, W. Ji, X. Gong, X. Wu, H. Wang, J. Chang Biomater. Sci. 2018, 6, 1379-1389.
31. A. Topete, D. Melgar, M. Alatorre-Meda, P. Iglesias, B. Argibay, S. Vidawati, S. Barbosa, J. A. Costoya, P. Taboada, V. Mosquera J. Mater. Chem. B, 2014, 2, 6967-6977.
32. S. Cotton, Lanthanide and Actinide Chemistry, J. Wiley & Sons., Ltd, Rutland, UK, 2006.
33. Dexter, D. L. *J. Chem. Phys.* **1953**, *21* (5), 836–850.
34. Förster, T. *Ann. Phys.* **1948**, *437* (1–2), 55–75.
35. Bettencourt-Dias, A. *Curr. Org. Chem.* **2007**, *11* (16), 1460–1480.
36. A. Brandner, T. Kitahara, N. Beare, C. Lin, M. T. Berry and P. S. May, *Inorg. Chem.* **2011**,
37. J. C. G. Bünzli, S. V. Eliseeva, in *Comprehensive Inorganic Chemistry II (Second Edition): From Elements to Applications*, Elsevier **2013**, 8, 339–398.
38. L. Armelao, G. Bottaro, S. Quici, C. Scalera, M. Cavazzini, G. Accorsi, Coord. Chem. Rev., 254 (2010) 487

39. Attarwala AA, Molina-Duran F, Bu¨sing K-A, Scho¨nberg SO, Bailey DL, et al. (2014) Quantitative and Qualitative Assessment of Yttrium-90 PET/CT Imaging. PLoS ONE 9(11): e110401. doi:10.1371/journal.pone.0110401
40. Hong-Shang Peng and Daniel T. Chiu Chem Soc Rev. 2015 July 21; 44(14): 4699–4722. doi:10.1039/c4cs00294f.
41. F. Meng, J. Wang, Q. Ping, Y.Yeo *ACS Nano* **2018**, 12, 6458−6468.
42. B. Andreiuk, A. Reisch, V. G. Pivovarenko, A. S. Klymchenko *Mater. Chem. Front*. **2017**, 1, 2309.
43. F. Piccinelli, A. Speghini, M. Monari, M. Bettinelli. *Inorg. Chim. Acta* **2012**, 385, 65–72.
44. F. Piccinelli, C. De Rosa, A. Melchior, G. Faura, M. Tolazzi, M. Bettinelli. *Dalton Trans.* **2019**, in press, DOI: 10.1039/C8DT03621G. 26.
45. M. Leonzio, M. Bettinelli, L. Arrico, M. Monari, L. Di Bari, F. Piccinelli *Inorg. Chem.* **2018**, 57, 10257−10264.
46. M. Mihorianu, M. Leonzio, M. Bettinelli, F. Piccinelli *Inorg. Chim. Acta* **2015**, 438, 10–13.
47. Nicolò Lanza's thesis "Progettazione ed implementazione di un tool di analisi di immagini con applicazione alla microscopia a forza atomica (AFM)"
48. D. F. Eaton, *Pure Appl. Chem.*, 1988, **60**, 1107–1114
49. D. Parker, P. K. Senanayake and J. A. G. Williams, *J. Chem. Soc. Perkin Trans. 2*, 1998, 2129–2140. C. Li, Y. Liu, Y. Wu, Y. Sun and F. Li, *Biomaterials*, 2013, **34**, 1223–1234

Appendix

Status: submitted to publication

Complexes of rare earth ions embedded in Poly(lactic-co-glycolic acid) (PLGA) nanoparticles: Characterization and spectroscopic study

Salvatore Calogero Gaglio,[1] Chiara De Rosa,[2] Fabio Piccinelli,[2]* Alessandro Romeo[3] and Massimiliano Perduca[1]

[1] Biocrystallography and Nanostructure laboratory, Department of Biotechnology, University of Verona, Strada Le Grazie 15, 37134 Verona, Italy

[2] Laboratorio Materiali Luminescenti, DB, Università di Verona, and INSTM, UdR Verona, Strada Le Grazie 15, 37134 Verona, Italy

[3] Laboratory for Photovoltaics and Solid State Physics, Department of Computer Science, University of Verona, Strada Le Grazie 15, 37134 Verona, Italy

Keywords

Poly(lactic-co-glycolic acid) (PLGA), nanoparticles, Eu(III), luminescence, Y(III), optical imaging, PET contrast agent.

Abstract

Several Eu(III) complexes [(Eu(**L1**)(tta)$_2$(H$_2$O)]·CF$_3$SO$_3$, Eu(**L2**)(NO$_3$)$_3$ and Eu(**L3**) with **L1** = *N, N'-bis(2-pyridylmethylidene)-1,2-(R,R+S,S)-cyclohexanediamine*, **L2** = *N, N'-bis(2-quinolylmethylidene)- 1,2-(R,R+S,S)-cyclohexanediamine*, **L3** *N-quinolyl-N,N',N'-trans-l,2-cyclohexylenediaminetriacetic acid* and tta = *2-thenoyltrifluoroacetyl-acetonate*] and one Y(III) complex [(Y(**L1**)(tta)$_2$(H$_2$O)]·CF$_3$SO$_3$] have been embedded, with a different degree of efficiency, in Poly(lactic-co-glycolic acid) (PLGA) matrix by using two different composition [Poly(lactic(50%)-co-glycolic acid(50%), briefly PLGA 50:50 and Poly(lactic(75%)-co-glycolic acid(25%), briefly PLGA 75:25], giving nanoparticles characterized by a monodispersed distribution of the size (diameter around 200 nm). The (Eu(**L1**)(tta)$_2$(H$_2$O)]·CF$_3$SO$_3$ shows the most efficient Eu(III) luminescence (F_{Tot} = 25%) when embedded in PLGA 75:25. The release of the complex

over the time in aqueous buffered solution has been followed by means of the decrease of Eu(III) luminescence and it is faster upon increasing the temperature to 37°C, in particular for the PLGA 50:50 system, whose melting temperature (Tm) is lower (33°C) than both the Tm of PLGA 75:25 (38°C) and the basal one.